M 2023

U. PORTO
FEUP FACULDADE DE ENGENHARIA
UNIVERSIDADE DO PORTO

DESIGN OF A NOVEL RACEWAY POND REACTOR FOR WASTE ACTIVATED SLUDGE ADVANCED PRE-TREATMENT TO FOSTER BIOGAS PRODUCTION

MARGARIDA DA LUZ RAZÃO PEIXOTO
MASTER THESIS IN CHEMICAL ENGINEERING
PRESENTED TO THE FACULTY OF ENGINEERING
OF THE UNIVERSITY OF PORTO

Master in Chemical Engineering

Design of a novel raceway pond reactor for waste activated sludge advanced pre-treatment to foster biogas production

Master dissertation

of

Margarida da Luz Razão Peixoto

Developed within the course of dissertation

held in

LSRE-LCM - Laboratory of Separation and Reaction Engineering - Laboratory of Catalysis and Materials

Supervisor at FEUP: **Vítor Jorge Pais Vilar, Principal Researcher at LSRE-LCM**

Joint supervisors at FEUP: **Ricardo Nogueira dos Santos, Auxiliary Researcher at LSRE-LCM**

Margarida Abrunhosa de Brito, Doctoral Researcher at LSRE-LCM

FEUP FACULDADE DE ENGENHARIA UNIVERSIDADE DO PORTO

DEPARTAMENTO DE ENGENHARIA QUÍMICA

July 2023

Agradecimentos

Tenho plena noção que a realização deste trabalho não seria possível sem a ajuda de várias pessoas, às quais gostaria de agradecer de forma particular.

Em primeiro lugar gostaria de agradecer aos meus orientadores. Ao Doutor Vítor Vilar pelos conselhos, pelos recursos disponibilizados e por todo o conhecimento transmitido. Ao Doutor Ricardo Santos pelo constante apoio e incentivo, pela boa disposição, por dar resposta a todas as minhas perguntas e por todas as ideias que permitiram enriquecer o meu conhecimento e, por conseguinte, o trabalho desenvolvido. À Margarida pela atenção e dedicação, por se mostrar sempre disponível para ajudar e por todas as sugestões que possibilitaram aprimorar o meu trabalho. Agradeço também por me darem a oportunidade de fazer parte deste grupo e por terem acreditado e confiado em mim para realizar este projeto.

Não posso deixar de agradecer à Carolina pela preciosa e paciente ajuda no desenho da geometria da *raceway* com inclinação em AutoCAD. Agradeço igualmente à Carla pela ajuda no laboratório e à Joana pelo fornecimento dos dados experimentais essenciais à realização deste trabalho.

Gostaria de agradecer igualmente à minha família, em especial aos meus pais, pela paciência, pelo apoio incondicional, e por todos os sacrifícios que fizeram e continuam a fazer por mim. Ao meu irmão, por me encorajar nos momentos mais difíceis e por acreditar sempre em mim. Aos meus avós por serem um exemplo e pelo orgulho que demonstram no meu percurso. À minha prima Inês por me incentivar desde o primeiro dia e por estar sempre presente em todos os momentos.

Agradeço também a todos os meus amigos que tornaram este percurso único. Agradeço em especial à Magui, por ser a minha confidente e companheira de estudo ao longo destes 5 anos e por todas as memórias e aventuras juntas.

Agradeço igualmente aos meus colegas de gabinete. À Laura e à Teresa pela interajuda, pela partilha de ideias e pela motivação. Ao Eduardo, à Carolina, à Sofia e à Isabel pelas dicas, conselhos e por mostrarem sempre disponibilidade para ajudar.

Finalmente, gostaria de agradecer a todas as pessoas que, não estando aqui citadas, contribuíram de uma forma ou de outra para a realização deste trabalho.

Dr. Vítor Vilar, Dr. Ricardo Santos, and Dr. Margarida Brito, supervisors of this dissertation, are members of LSRE-LCM - Laboratory of Separation and Reaction Engineering – Laboratory of Catalysis and Materials, financially supported by LA/P/0045/2020 (ALiCE), UIDB/50020/2020 and UIDP/50020/2020 (LSRE-LCM), funded by national funds through FCT/MCTES (PIDDAC).

REPÚBLICA PORTUGUESA

FCT Fundação para a Ciência e a Tecnologia

Abstract

According to the new European Union (EU) Directive, the water treatment sector must become energy neutral by 2040. Therefore, increasing biogas production in Wastewater Treatment Plants (WWTPs) is of utmost importance. To this end, several pre-treatments of waste activated sludge (WAS) that aim to enhance the hydrolysis step in anaerobic digestion (AD) have been studied. However, cost-efficiency pre-treatment techniques have not yet been established. In this sense, raceway pond reactors (RPRs) are a promising solution to this problem. This work assessed the design of RPRs and the study of some parameters that affect their performance in sludge disintegration.

The approach used for the computational simulation consisted in dividing the 3D domain into several 2D subdomains, thereby reducing the computational resources.

Firstly, the global performance of the reactor was studied, analysing the influence of the implementation of flow deflectors in the reactor U-turn. It has been demonstrated that the installation of these baffles promotes the uniformity of the flow, reducing the secondary flow and, consequently, the energy dissipation. Additionally, the pressure drop proved to be much lower, which contributes to a lower energy consumption in the process.

Afterwards, the vertical flow in the reactor was studied, encompassing the analysis of wall roughness, level of vertical mixing, shear stresses in the flow and radiation. It has been found that, at certain conditions, the reactor presents a good degree of vertical mixing, as the velocity in the direction of solar light incidence was high enough to keep the particles in constant motion. In addition, the probability density function of the particles' y-position exhibits an approximately homogeneous distribution. Regarding the radiation analysis, it has been observed that a large amount of energy can be obtained after a treatment cycle, which is sufficient to promote a high level of sludge disintegration. Furthermore, the treatment time can be adapted depending on the intensity of the incident radiation and the required disintegration level.

Lastly, the circulation of the fluid in the reactor was assessed, comparing the efficiency of two propulsion components, a paddlewheel and an inclined system coupled with a pump and a distributor. The paddlewheel impeller turned out to have a lower energy consumption, even though its efficiency is rather low. Besides that, it was concluded that using longer blades than the liquid height is advantageous and results in improved efficiency.

This work offers design guidelines for novel RPRs applied to the pre-treatment of WAS. These guidelines cover the different components involved in the reactor system, providing valuable insights for its efficient design and implementation.

Keywords: Computational Fluid Dynamics, Raceway Pond Reactor, Waste Activated Sludge, Pre-treatment, WWTP.

Resumo

De acordo com a nova Diretiva da União Europeia, o setor de tratamento de águas deve tornar-se energeticamente neutro até 2040. Assim, o aumento da produção de biogás nas Estações de Tratamento de Águas Residuais (ETARs) é de extrema importância. Para tal, vários pré-tratamentos de lamas ativadas que visam melhorar a eficiência da etapa de hidrólise na digestão anaeróbia têm vindo a ser estudados. No entanto, ainda não se estabeleceram técnicas de pré-tratamento com um bom compromisso entre eficiência e custo. Neste sentido, os reatores *raceway* são uma solução que se revela promissora para este problema. Neste trabalho, o projeto destes reatores e o estudo de alguns parâmetros que afetam o seu desempenho na desintegração das lamas foi avaliado.

A estratégia utilizada para a simulação computacional consistiu em dividir o domínio 3D em vários subdomínios 2D, reduzindo assim os recursos computacionais.

Desta forma, primeiramente estudou-se o desempenho global do reator, analisando a influência da implementação de defletores na curva em U do mesmo. Ficou demonstrado que a instalação destes defletores promove a uniformidade do escoamento, reduzindo o escoamento secundário e, por conseguinte, a dissipação de energia. Adicionalmente, a queda de pressão revelou-se bastante menor, o que contribui para um menor consumo energético no processo.

De seguida, estudou-se o escoamento vertical no reator, englobando a análise da rugosidade das paredes, do nível de mistura vertical, das tensões de corte no escoamento e da radiação. Verificou-se que nas condições em estudo o reator apresenta um bom grau de mistura vertical, uma vez que a velocidade na direção de incidência da luz solar se mostrou suficientemente elevada para manter as partículas em constante movimento. Além disso, a função densidade de probabilidade da posição y das partículas apresenta uma distribuição aproximadamente homogénea. Relativamente à análise da radiação, constatou-se que é possível obter grandes quantidades de energia ao fim de um ciclo de tratamento, sendo suficiente para promover um elevado nível de desintegração das lamas. O tempo de tratamento pode ser adaptado dependendo da intensidade da radiação incidente e do nível de desintegração desejado.

Por último, analisou-se a circulação do fluído no reator, tendo-se comparado a eficiência de dois componentes propulsores, uma roda de pás e um sistema inclinado acoplado com uma bomba e um distribuidor. O impulsor por roda de pás acabou por revelar um menor consumo energético, no entanto a sua eficiência é bastante baixa. Além disso, concluiu-se que utilizar um comprimento de pás superior à altura de líquido é vantajoso e resulta numa eficiência superior.

Este trabalho fornece, portanto, diretrizes de projeto para novos reatores *raceway* aplicados ao pré-tratamento de lamas ativadas, englobando os vários componentes do mesmo.

Palavras-chave: Dinâmica de Fluídos Computacional, Reator *raceway*, Lamas ativadas, Pré-tratamento, ETAR.

Declaration

I hereby declare, under word of honour, that this work is original and that all non-original contributions are indicated, and due reference is given to the author and source.

Margarida da Luz Razão Peixoto

Margarida da Luz Razão Peixoto

July 2023

Index

1 Introduction 1
1.1 Framing and presentation of the work 1
1.2 Contribution of the author to the work 2
1.3 Organization of the dissertation 2
2 Context and State of the Art 3
2.1 Wastewater treatment plant (WWTP) 3
2.1.1 Anaerobic Digestion and Waste Activated Sludge 4
2.1.2 Biogas 5
2.2 Pre-treatment techniques 6
2.2.1 Physical/Mechanical Pre-Treatments 6
2.2.2 Thermal Pre-Treatments 7
2.2.3 Chemical Pre-Treatments 8
2.2.4 Biological Pre-Treatments 9
2.2.5 Concluding Remarks 9
2.3 Raceway Pond Reactors 9
3 Numerical Methods 13
3.1 Governing Equations 13
3.1.1 RANS Equations 13
3.1.2 Standard k-ε model 14
3.1.3 Transport equation 15
3.1.4 Discrete Phase Model 15
3.1.5 VOF Model 16
4 Overall Flow Design 19
4.1 CFD Model 19
4.1.1 Geometry 19
4.1.2 Boundary and Initial Conditions 19
4.1.3 Models and Solution Methods 20

4.1.4 Mesh 20
4.2 Results 21
4.2.1 Mesh Independence Test 21
4.2.2 RPR Flow Deflectors Design 24
5 Vertical Flow 27
5.1 CFD Model 27
5.1.1 Geometry and Mesh 27
5.1.2 Boundary Conditions 27
5.1.3 Solution Methods 28
5.2 Results 28
5.2.1 Rugosity and Δp Assessment 28
5.2.2 Turbulence Distribution 29
5.2.3 Vertical Mixing 30
5.2.4 Turbulent shear stresses 33
5.2.5 Radiation Analysis 33
6 Flow Circulation 35
6.1 CFD Model 35
6.1.1 Geometry 35
6.1.2 Boundary Conditions 35
6.1.3 Solution methods 36
6.1.4 Mesh 36
6.2 Results 37
6.2.1 Power Consumption 37
6.2.2 Paddlewheel vs Pump Recirculation 40
7 Conclusion 43
8 Assessment of the work done 45
8.1 Objectives Achieved and Future Work 45
8.2 Final Assessment 45
9 References 47

Appendix A – Mesh independence test 51

Appendix B - Δp assessment 53

Appendix C – Stoke's law 55

Appendix D – Probability Density Function 57

Appendix E - UVA spectrum 59

Appendix F - Sliding mesh model 61

Appendix G - Torque 63

List of Figures

Figure 1. WWTP process flow diagram. 3

Figure 2. Velocity profiles: Traditional (top), Isle Partition (middle) and Baffles Partition (bottom). Reprinted with permission from Inostroza et al. [54]. Copyright 2021. Elsevier. 11

Figure 3. Diagram of the RPR with sloping baffles and flow deflectors. Reprinted with permission from Huang et al. [59]. Copyright 2015. Elsevier 11

Figure 4. Geometry of the 2D domain. 19

Figure 5. Flowrate streamlines of meshes 05, 03, 025, 02 and 018. 21

Figure 6. Turbulent kinetic energy, k, of meshes 05, 03, 025, 02 and 018. 22

Figure 7. Turbulent dissipation rate, ε, of meshes 05, 03, 025, 02 and 018. 22

Figure 8. Total pressure difference, Δp, and wall shear stresses, τ, for each mesh studied. 23

Figure 9. Mesh02 details for different zones. 23

Figure 10. Flow deflectors 2D geometry. 24

Figure 11. Mesh details for flow deflectors zone. 25

Figure 12. Flowrate streamlines before, ND, and after the implementation of flow deflectors for the different configurations studied. 25

Figure 13. Velocity profiles at the outlet for the different RPR deflectors configurations. 26

Figure 14. RRP Depth Plan 2D Geometry. 27

Figure 15. Average velocity dependence on roughness constant and roughness height. 29

Figure 16. Map of turbulent kinetic energy. 29

Figure 17. Map of turbulent energy dissipation rate. 30

Figure 18.Contour plots of mass fraction of tracer. 32

Figure 19. PDF of particles' y position. 32

Figure 20. Radiation profile over the sludge depth. 34

Figure 21. Rotary machine 2D geometry. 35

Figure 22. Mesh details of the paddlewheel geometry domain. 37

Figure 23. Mass flowrate of water, left, and moment of the force exerted on the paddle walls, right, for the different values of L_p simulated. 38

Figure 24. Volume fraction of water for Padd2 geometry over time. 39

Figure 25. Sloped geometry perspective view. 40

Figure 26. RPR Design Diagram. *44*

Figure 27. Velocity, u*, and wall shear stresses,* τ*, for each mesh studied.* *51*

Figure 28. Comparison between Fluent and Manning's equation velocity. *53*

Figure 29. UVA spectrum of WAS for the two tests performed. *59*

Figure 30. Moment about a specified moment centre. *63*

List of Tables

Table 1. Element sizes and number of elements for each mesh studied. 21

Table 2. Total pressure difference, Δp, and wall shear stresses, τ, for each mesh studied. 23

Table 3. Element size, number of elements, Δp and τ for each mesh evaluated. 24

Table 4. Values of x_1, x_2, L_1 and L_2 for each design point analysed. 25

Table 5. Dimensions of the paddlewheel computational domain for the two cases studied. 35

Table 6. Results and efficiency of each paddlewheel studied. 39

Table 7. Element size, number of elements, velocity, u, and wall shear stresses, τ, for each mesh studied. 51

Notation and Glossary

A	Area	m^2
A_b	Absorbance	
C	Pipeline roughness coefficient	
Co	Courant number	
$C_{1\varepsilon}$, $C_{2\varepsilon}$, $C_{3\varepsilon}$	k-ε turbulence model constants	
C_D	Drag coefficient	
C_μ	Turbulent viscosity constant	
d	Inside pipe diameter	m
d_p	Particle diameter	m
$D_{n,m}$	Mass diffusion coefficient for species *n* in the mixture	$m^2 \cdot s^{-1}$
D_t	Turbulent diffusivity	$m^2 \cdot s^{-1}$
$D_{T,n}$	Thermal diffusion coefficient	$m^2 \cdot s^{-1}$
E_t	Total energy received by WAS during a treatment cycle	$J \cdot m^{-2}$
F	Additional force	N
F_i	External force	$N \cdot m^{-3}$
F_D	Drag force	N
F_p	Pressure force vector	N
Fr	Dimensionless Froude number	
F_v	Viscous force vector	N
g	Acceleration of gravity	$m \cdot s^{-2}$
G_b	Generation of turbulent kinetic energy due to the buoyancy	
G_k	Generation of turbulent kinetic energy due to the mean velocity gradients	
h	Sludge depth	m
h_f	Pipeline friction losses	m
h_m	Pipeline minor losses	m
h_p	Height of the paddlewheel computational domain	m
i_s	Isoline slope	
I	Intensity of radiation	$W \cdot m^{-2}$
I_0	Intensity of incident radiation	$W \cdot m^{-2}$
J_n	Diffusion flux of species *n*	$kg \cdot m^{-2} \cdot s^{-1}$
k	Turbulent kinetic energy	$m^2 \cdot s^{-2}$
k_n	Unit matching constant	
K	Loss coefficient	
l	Additional height considered for the collector tank	m
l_b	Width of the spectrophotometer cuvette	m
L	Length of the rectangular section of the RPR depth plan	m
L_f	Length of the pipe	m
L_{in}	Inlet dimension of the RPR	m
L_m	Distance between the two channels of the RPR	m
L_{out}	Outlet dimension of the RPR	m
L_r	Total length of the RPR	m
L_w	Side wall length of the RPR	m
L_1, L_2	Flow deflectors length design parameters	m
L_p	Length of the paddlewheel computational domain	m
m_p	Discrete particle mass	kg
$\dot{m}_{LG}$	Mass transfer from the liquid phase to the gas phase	$kg \cdot m^{-3} \cdot s^{-1}$
$\dot{m}_{GL}$	Mass transfer from the gas phase to the liquid phase	$kg \cdot m^{-3} \cdot s^{-1}$
n	Time level	
N	Rotation velocity	rpm
n_r	Manning coefficient of roughness	

p	Pressure	Pa
p_{ref}	Reference pressure	Pa
$P(y)$	Probability that the y position of a particle assumes a value between a specified range	
P_f	Power received by the fluid	W
P_s	Power supplied by the paddlewheel	W
q	Volume flowrate	$m^3 \cdot s^{-1}$
r	Radius of the particle	m
R	Bend radius of the RPR	m
R_h	Hydraulic radius	m
R_n	Net rate of production of species n by chemical reaction	$kg \cdot m^{-3} \cdot s^{-1}$
R_p	Paddlewheel radius	m
$\mathrm{Re_r}$	Relative Reynolds number	
S	Manning's equation slope	
$\mathrm{Sc_t}$	Schmidt number	
S_k	Source term of the transport equation for turbulent kinetic energy	$kg \cdot m^{-1} \cdot s^{-3}$
S_ε	Source term of the transport equation for turbulent dissipation rate	$kg \cdot m^{-1} \cdot s^{-4}$
$s_{ij}{}'$	Fluctuating strain rate tensor	s^{-1}
S_{ij}	Mean strain rate tensor	s^{-1}
S_n	Transport equation source term	$kg \cdot m^{-3} \cdot s^{-1}$
t	Time	s
t_c	Duration of a treatment cycle	s
T	Temperature	K
T_r	Torque	N·m
T_t	Observation time	s
T_y	Total amount of time that a particle falls in a specified range	s
u	Velocity magnitude	$m \cdot s^{-1}$
u_p	Particle velocity	$m \cdot s^{-1}$
u_{max}	Maximum fluid velocity	$m \cdot s^{-1}$
v_p	Velocity inside the pipe	$m \cdot s^{-1}$
V	Volume	m^3
x, y, z	Axial coordinates	m
x_1, x_2	Flow deflectors width design parameters	m
y^+	Wall y plus	
y^*	Wall y star	
y_b	Distance from the bottom to the free-surface	m
Y_n	Local mass fraction of each n^{th} *specie*	
Y_M	Contribution of the fluctuating dilation in compressible turbulence to the overall dissipation rate	
w_r	Total width of the RPR	m

Greek Letters

ε	Turbulent dissipation rate	$m^2 \cdot s^{-3}$
μ	Molecular viscosity	Pa·s
μ_f	Viscosity of the fluid	Pa·s
μ_t	Eddy or turbulent viscosity	Pa.s
ρ	Density	$kg \cdot m^{-3}$
ρ_p	Density of the particle	$kg \cdot m^{-3}$
ρ_f	Density of the fluid	$kg \cdot m^{-3}$
σ_k	Prandtl number of k	
σ_ε	Prandtl number of ε	
α_L	Volume fraction of liquid	
α_G	Volume fraction of gas	
δ_{ij}	Kronecker delta	
Δp	Pressure difference	Pa

Δt	Time interval	s
Δx	Mesh element size	m
φ	Scalar quantity	
ω	Angular velocity	rad·s^{-1}
τ	Wall shear stresses	Pa
τ_{ij}	Reynolds stresses	Pa
τ_p	Residence time	s
τ_r	Relaxation time	s
τ_s	Cells tensile strength	Pa
$\tau_{vertical}$	Time it takes for a fluid element to travel through the vertical section of the RPR	s
v_t	Particles' settling velocity	m·s^{-1}
η	Efficiency factor	%

Indexes

*	dimensionless variable
i, j, l	index associated with the x, y and z cartesian components
$\bar{}$	Mean
$'$	Fluctuating component

List of Acronyms

2D	Two Dimensional
3D	Three Dimensional
AD	Anaerobic Digestion
AP	Alkaline Pre-treatment
BOD	Biochemical Oxygen Demand
CFD	Computational Fluid Dynamics
CFL	Courant-Friedrichs-Lewy
COD	Chemical Oxygen Demand
DPM	Discrete Phase Model
DRW	Discrete Random Walk
EPS	Extracellular Polymeric Substance
EU	European Union
PBC	Periodic Boundary Condition
PDF	Probability Distribution Function
PRESTO!	Pressure Staggering Option
RANS	Reynolds Average Navier Stokes
RPR	Raceway Pond Reactor
SCADA	Supervisory Control and Data Acquisition
TS	Total Solids
UVA	Ultraviolet A
VOF	Volume of Fluid
WAS	Waste Activated Sludge
WWTP	Wastewater Treatment Plant

1 Introduction

1.1 Framing and presentation of the work

The search for alternative energy sources is becoming crucial in today's world. This need has to do with the depletion of fossil resources, but mainly with environmental issues, such as the harmful effects of greenhouse gases. In this context, improving renewable energy production has become mandatory. Moreover, rapid urbanisation means that more and more waste is being generated. A very concrete example is wastewater treatment plants (WWTPs). Sludge generated at WWTPs could yield substantial energy in the form of biogas, if captured and managed efficiently [1, 2].

WWTPs are one of the largest consumers of energy in the public sector. According to the EU Urban Wastewater Treatment Directive, the wastewater sector must become energy-neutral by 2040 [3]. Thus, biogas production has a prominent role in complying with this Directive.

Primary and secondary sludge are the main byproducts of WWTPs. Commonly, this sludge is treated by anaerobic digestion (AD), which is one of the most efficient and sustainable treatments for this purpose. While primary sludge is quite biodegradable, secondary sludge or waste activated sludge (WAS) is difficult to degrade due to its complexity. WAS is regarded as a cluster of organic components, whose presence hinders AD hydrolysis. This problem results in longer retention times, lower biogas yields, and the need to use a larger bioreactor. Therefore, pre-treatment of WAS becomes necessary to accelerate the hydrolysis rate and increase AD efficiency [4].

In the last years, some pre-treatments have been studied, including mechanical, chemical, thermal, and biological processes. However, efforts are currently underway to establish sustainable and cost-effective pretreatment methods. Physical treatments require a large amount of energy. In chemical treatments, the biggest challenge is the balance of the reactor pH, since it can inhibit AD performance and may require more expensive materials tolerant to acidic conditions. An important issue in biological processes is maintaining optimal conditions for the microorganisms, which may require high installation costs. Moreover, thermal pretreatments are an energy-intensive solution [4].

Raceway pond reactors (RPRs) are extensive non-concentrating photoreactors with a very low construction cost consisting of open channels forming a raceway where a liquid stream is set in motion. They have been used for solar applications like microalgal mass culture and urban wastewater disinfection using a photo-Fenton reaction [5, 6]. Nevertheless, its application for WAS pre-treatment was never evaluated. This work proposes the development of a RPR for pre-treatment of WAS from WWTPs in order to induce thermal/photochemical/chemical reactions, disintegrating the cellular membrane of bacterial cells and subsequent release of their organic content into the solution. This will accelerate the hydrolysis stage of the WAS in AD, boosting biogas production and quality, promoting sludge stabilization, and enabling its use as nutrient-rich biosolids for crops growth and soil structure.

The RPR design and some chemical/physical aspects that affect WAS disintegration will be analysed using Computational Fluid Dynamics (CFD). Many studies in the literature have used CFD since it is a powerful tool that enables characterising/assessing numerous essential variables that are typically challenging to measure through experimental means [5].

1.2 Contribution of the author to the work

The numerical CFD simulations and the building of the geometries and meshes were performed by the author of this work with the guidance of the supervisors. The WAS absorbance was measured with the aid of a PhD student, Carla Santos. A PhD student, Joana Monteiro, provided information regarding the sludge particle diameter and the total solids content. The AutoCAD sloped geometry was designed with the aid of Maria Carolina Duarte.

1.3 Organization of the dissertation

This work is divided into 8 chapters briefly described hereinafter:

The objective of Chapter 1 is to introduce the problem in a global context and to present the main concepts of this work.

Chapter 2 aims to summarise the main problems associated with biogas and the limiting step of AD in WWTPs (Section 2.1). Additionally, a review of the pre-treatment techniques already studied is presented (Section 2.2). Finally, past studies regarding the application of CFD for the design of RPRs are described (Section 2.3).

In Chapter 3 the numerical methods including the governing equations used in this work are described.

Chapter 4 comprises the study of the overall flow design. First, the CFD model, regarding the physical domain (Section 4.1.1), boundary conditions (Section 4.1.2), solution methods (Section 4.1.3), and mesh (Section 4.1.4) is explained. Then, the results, including the grid independence test (Section 4.2.1) and the setup of flow deflectors in the RPR (Section 4.2.2), are provided.

Chapter 5 addresses the analysis of the vertical flow in the RPR. The CFD model is described in Section 5.1, while the results, including the rugosity and Δp assessment, the turbulence distribution, the vertical mixing, the turbulent shear stresses, and the radiation analysis are in Section 5.2.

Chapter 6 presents the study of the flow circulation system. The CFD model is detailed in Section 6.1. In addition, the power consumption of a paddlewheel impeller and its comparison with a sloped geometry propelled by a pump is shown in Section 6.2.

Chapters 7 and 8 present the conclusions and the assessment of the work done, respectively.

2 Context and State of the Art

2.1 Wastewater treatment plant (WWTP)

A WWTP is an industrial facility that combines physical, mechanical, chemical, and biological processes. It is used to remove various contaminants from the influent wastewater, providing treated water with quality suitable for reuse or to be discharged back into the environment [7]. Thereby, it seems clear that WWTPs play a crucial role in environmental preservation.

The wastewater treatment process involves two phases, liquid and solid, as shown in Figure 1. Domestic and industrial wastewater, mostly contaminated with organic matter, solids, and nutrients, are first subject to a preliminary treatment. This treatment stage is designed to remove larger solids, grit, grease, and oils from wastewater. After that, the liquid phase proceeds to the primary treatment. This treatment is responsible for removing suspended solids and organic matter from the effluent. Primary treatment is followed by secondary treatment, where the liquid phase undergoes a biological process. It is based on the growth of microorganisms, referred to as biomass. The liquid phase treatment is completed with the tertiary treatment (typically required during the bathing season), which is designed to decrease the content of suspended solids and disinfect the effluent, by means of micro screening and ultraviolet radiation [8].

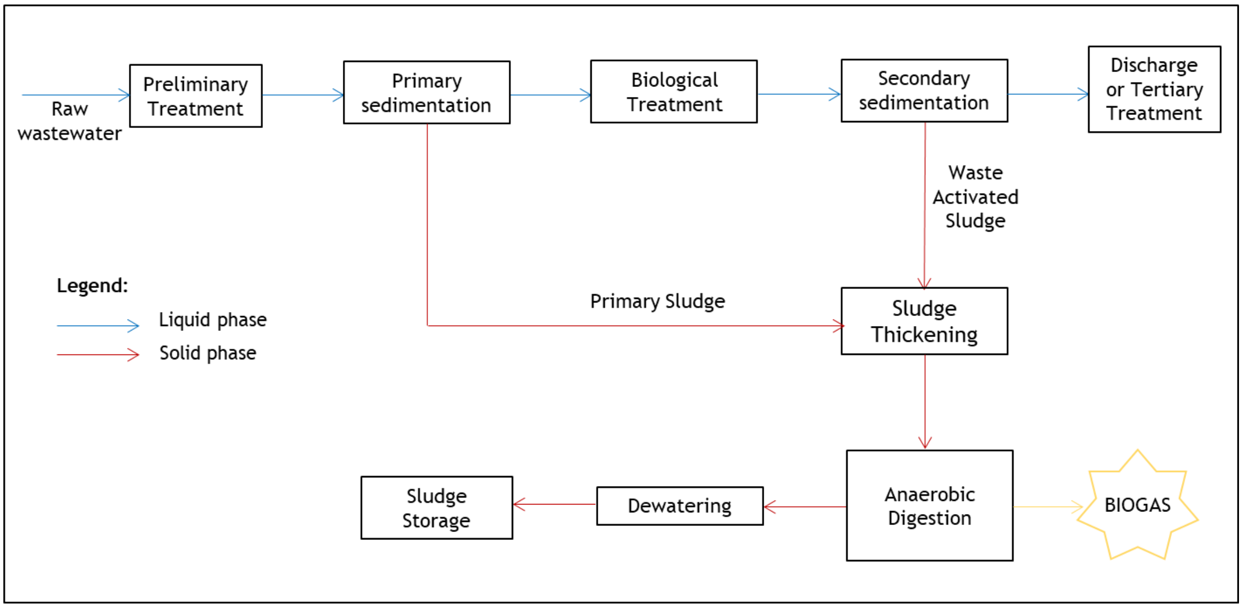

Figure 1. WWTP process flow diagram.

Regarding the solid phase, primary sludge is produced in the primary settler by gravitational sedimentation. It is easy biodegradable, having a high content of organic matter. The secondary sludge, also named as waste activated sludge, results from the biological treatment and has a more complex composition [8]. Both primary and secondary sludge undergo a thickening process.

After that, they proceed to AD. The aim is to stabilize and reduce the organic matter content by about 50 % and to produce a biofuel known as biogas. This sludge is then converted into a dewatered and stabilized sludge [8].

2.1.1 Anaerobic Digestion and Waste Activated Sludge

AD is considered as an efficient, effective and sustainable remediation technique, making it one of the most widely used processes for sewage sludge treatment. It is a process through which bacteria break down organic matter into simple soluble compounds in an anaerobic environment. The main goals of AD are to stabilize organic matter, reduce sludge volume, inactivate pathogens, and reduce chemical and biochemical oxygen demand (COD and BOD, respectively), which is achieved by converting wastewater organics to methane and carbon dioxide using microorganisms [9]. Otherwise, AD is a slow process and very sensitive to the operation conditions, such as temperature pH, organic load and carbon to nitrogen, C/N, ratio. [10].

AD involves four stages: hydrolysis, acidogenesis, acetogenesis, and methanogenesis. Hydrolysis breaks down insoluble organic matter and high molecular weight compounds (proteins, lipids, polysaccharides) into soluble substances, namely fatty and amino acids. However, it is considered as a rate-limiting step. Acidogenesis further splits the hydrolysis products, forming volatile fatty acids with ammonia, hydrogen sulfide, carbon dioxide, and other byproducts. The third stage in AD, acetogenesis, is responsible for the digestion of the larger chain organic acids and alcohols to produce acetic acid and minor quantities of carbon dioxide and hydrogen. The last stage is methanogenesis, where methanogenic bacteria form methane gas: one group breaks down acetate into carbon dioxide and hydrogen and the other produces methane by using carbon dioxide as an electron acceptor and hydrogen as a donor [11].

WAS is mostly composed of bacterial cells, inorganic substances (such as grit and heavy metals), adsorbed organic matter (lipids, humic substances, polysaccharides and proteins), and extracellular polymeric substances (EPSs). These components can interact with each other to form a semi-rigid structure. According to several studies, in terms of % volatile solids, WAS is composed of 25-62.4 % proteins; 7.7-28.6 % humic substances; 10-24 % bacterial biomass; 7-19 % carbohydrates, and <3.5 % DNA [4]. Thus, it can be deduced that WAS mainly consists of proteins and humic substances with bacterial mass and carbohydrates in smaller proportions. The presence of humic substances poses a challenge during AD, as they are difficult to degrade anaerobically and affect enzymatic activity, which, thereby lowers biodegradability [12]. On the other hand, proteins, carbohydrates, and DNA are anaerobically degradable substances. However, their biodegradability seems to diminish when integrated into an organized structure like WAS [4]. Thus, the sludge properties and structure hinder its bioconversion, decreasing the hydrolysis efficiency in AD. This results in lower methane conversion and consequent lower biogas yield.

One strategy that has been implemented in many WWTPs is co-digestion. It consists of mixing and treating together different substrates, such as food waste, animal manure, and plant material. Many studies report that this strategy increases organic matter biodegradation, enhancing biogas production [13]. Although, it has some disadvantages, such as the accumulation of solids in the digester, shorter hydraulic retention time, nitrogen backload, and reduced dewaterability [14]. Another strategy that has attracted worldwide attention is to implement WAS pre-treatment techniques. These pre-treatment techniques have been proven to rupture complex EPSs, reduce solid mass, increase soluble substrate amount, increase methane production during AD, and lower the overall cost of sludge management [9]. The present work will focus on this pre-treatment step. Some technologies already implemented will be further discussed.

2.1.2 Biogas

As energy consumption is increasing worldwide and resources are being depleted, sustainable energy production is of growing concern. Biogas production from sewage sludge is a promising technology that can reduce the environmental hazards of WAS, generate clean energy, and contribute to a circular economy.

Biogas contains about 50-75 % methane, 25-50 % carbon dioxide, and other gaseous impurities such as nitrogen, hydrogen, hydrogen sulphide, and oxygen [9]. It can be utilised to generate heat, provide electricity, and produce biomethane. The higher the methane content, the greater the calorific value of biogas, so improving the quality of this product also involves increasing the amount of methane in its constitution. In this sense, biogas produced from sewage sludge has some advantages, as it typically has a higher methane content compared to other feedstocks [15].

WWTPs are one of the most energy-intensive public industries, representing more than 1 % of total energy consumption in Europe [16]. To meet discharge standards, WWTPs consume a large amount of energy. Secondary treatment represents more than 70 % of this energy consumption, with aeration systems representing the vast majority of this expenditure (60 %), followed by pumping systems and anaerobic digestion. Biogas production in AD is beneficial and can cover part or all of the sludge treatment costs as well as the plant power consumption. It can be used to maintain the anaerobic digester at 35 °C (when the process is mesophilic) or 55 °C (when the process is thermophilic) and to generate energy for pumping systems, aeration blowers, and generators. In addition, it can be applied for sludge dewatering and for other WWTP heating facilities [17]. In this sense, besides being used to meet the calorific and energy requirements of the WWTPs, it can also be sold and represent an economic added value.

There are already some successful examples of WWTPs that have achieved energy neutrality. In Portugal, the WWTP of Guia in Lisbon reached this level in 2017. This achievement allowed saving around half a million euros and avoiding the emission of six thousand tons of carbon dioxide into the atmosphere per year. This was made possible through process optimization measures, including the cogeneration process, which enables the production of electricity from the biogas [18].

Another successful example comes from Denmark, from the Marselisborg treatment plant. This plant has not only achieved energy neutrality but has also produced an energy surplus of 53 %. It is important to highlight that this facility does not rely on solar or wind installations for energy generation, nor does it utilize additional materials like fat, oil, and grease from the food industry or sludge from other facilities. All the energy generated at the Marselisborg WWTP is derived exclusively from the treatment of regular household wastewater. This seemed extraordinary and was made possible by studying all the treatment phases of the process. Some of the measures implemented were integrating a Supervisory Control and Data Acquisition (SCADA) control system and replacing some equipment with more efficient ones [19].

2.2 Pre-treatment techniques

Pre-treatment techniques intend to make the sludge floc's structure more accessible, simplifying its composition and turning compounds available for microbial degradation in AD. During the last few years, many different pre-treatment methods with different operation modes and results have been reported. An overview of these techniques, including physical/mechanical, thermal, chemical, and biological processes is reported in the following subsections [4].

2.2.1 Physical/Mechanical Pre-Treatments

Physical pre-treatments are characterized by a physical force application. Thus, the substances are converted into smaller and more soluble compounds, which enables a greater surface area and, as such, a greater interaction between the substrate and the microorganisms present in the anaerobic digester [20]. The main drawbacks of it are associated with the requirement for high energy inputs. Among the various types of physical pre-treatments, ultrasonication, microwave irradiation, and high-pressure homogenisation stand out [21].

Ultrasonication

Ultrasonication consists of a cavitation process induced by ultrasound waves. The cavitation process is influenced by several parameters, such as ultrasound frequency, temperature, ultrasonic density, and total solids (TS) content [22]. Li et al. [23] reported that at a frequency of 20 kHz, a density of 0.5 $W \cdot mL^{-1}$, and sonification for 80 min, the methane production increased by 53.8 %. Regarding the solids content, Sahinkaya [24] achieved an optimum range of 2.3-3 %, to avoid loss of ultrasonic efficiency and increases in energy consumption. Lizama et al. [25] reported that higher specific energy input ($kJ \cdot [kg\ TS]^{-1}$) leads to higher biogas production. However, the opposite effect was observed above a certain limit (25 000 $kJ \cdot [kg\ TS]^{-1}$), which should be related to the formation of inhibitory and/or insoluble compounds due to the high temperatures and energy inputs. Furthermore, it was reported that at high energy inputs, the dewaterability of sludge is not favoured [26]. Thus, despite improving biogas production and the disintegration of WAS, the main disadvantages of ultrasonic pre-treatment are the high energy requirements/limitations and the need for lower solids concentration.

Microwave Irradiation

Microwave irradiation involves the use of high-frequency electromagnetic radiation to heat the sewage sludge and disrupt its cell structure [27]. Numerous studies have shown how microwave pre-treatment can help to improve the AD effectiveness of WAS. For example, a study by Appels et al. [27] showed that microwave pre-treatment under a specific energy input of 336 kJ·[kg TS]$^{-1}$ and 800 W of power resulted in a 214 % increase in sludge solubilization, as well as an increment of 50 % in biogas production compared to untreated sludge. Similarly to the ultrasonic pre-treatment, there is a positive effect between the increase in energy input and biogas production [28]. On the other hand, contrary to ultrasonication, some studies have shown that with increasing solids concentration, solubilisation increased, and the energy input was lower [29].

High-Pressure Homogenisation

High-pressure homogenisation (HPH) uses high pressure to disrupt cell walls and improve the digestibility of WAS [22]. Zhang et al. [30] found a positive trend between increasing pressure and sludge disintegration by applying homogenisation pressures from 20 MPa to 80 MPa. In contrast, the trend did not maintain with increasing TS concentration, and the sludge disintegration degree decreased. Furthermore, it was also concluded that the solubilisation of the sludge improved with the increase in the number of treatment cycles [30]. Regarding biogas production, Zhang et al. [30] reported an increment of 115 % after a 7-day AD, compared to untreated sludge. The authors have used a pressure of 50 MPa and two cycles of homogenization.

2.2.2 Thermal Pre-Treatments

Thermal pre-treatments are characterized by the application of heat at temperatures between 50 °C and 210 °C. For temperatures up to 100 °C, the process is named as low-temperature pre-treatment. Otherwise, the process is denominated as high-temperature pre-treatment [31].

High-Temperature

Regarding high-temperature pre-treatment, the majority of the studies in the literature report high levels of effectiveness for temperatures between 160-180 °C and treatment times between 20 and 40 minutes [21]. Carrère et al. [32] performed a study with temperatures between 60 °C and 210 °C. The authors found that, at temperatures up to 190 °C, sludge solubilisation, biodegradability, and methane generation increased. However, at 210 ºC, the authors reported undesired reactions that resulted in the formation of non-biodegradable high-molecular-weight compounds. Similarly, other studies have shown that very high temperatures resulted in the formation of recalcitrant substances, which despite being soluble, do not contribute to methane bioconversion [33, 34]. In addition, many studies reveal an improvement in dewaterability, especially at temperatures above 150 °C [35].

Low-Temperature

Due to the high energy expenditure and the potential for inhibitory or recalcitrant compounds to be formed at high temperatures, low-temperature pre-treatments have begun to be studied. Liao et al. [36] reported that COD solubilisation of high solids sludge (15 % TS) incremented with increasing temperature from 50 °C to 60 °C, 70 °C and 80 °C, after 30 minutes of pre-treatment. Furthermore, biodegradability and biogas production also increased. Biogas production increased by about 7.3 %, 15.6 %, and 24.4 % for temperatures of 60 °C, 70 °C, and 80 °C, respectively. In addition to temperature, the duration of the pre-treatment also proved to be a determining factor in its effectiveness. A research performed by Ruffino et al. [37] concluded that the COD solubilisation and the biogas production also rose with the treatment duration (1-15 h). Similarly, Liu et al. [38] concluded that at 90 °C, methane productivity increased 3-fold and 5-fold when sludge was pre-treated for 1 h and 36 h, respectively.

2.2.3 Chemical Pre-Treatments

Chemical pre-treatments comprise the use of reagents to disintegrate sludge's floc structure. Several chemical agents have been investigated, including alkaline, acid, and oxidizing (hydrogen peroxide, ozone, and Fenton's reagents) agents.

Alkaline

The main benefits of alkaline pre-treatment (AP) are related to a high pH, which can alter the sludge's structure, modifying the surface properties and the electrostatic charge of EPS [39]. The most used base solution corresponds to sodium hydroxide (NaOH), due to its effectiveness even at low dosages [40]. Shao et al. [41] have studied AP effectiveness at various pH values: 8, 9, 10, 11, and 12. Concerning biogas production, it was noticed an increase of 15.4 % compared to untreated sludge at pH 10. Nonetheless, with increasing alkalinity at pH 12, a decrement of 18.1 % was reported. This reduction could be related to the formation of refractory and poorly biodegradable compounds, like high-temperature pre-treatment.

Acid

In the acid pre-treatment, the pH value ranges from 1 to 5.5. The most used solutions are hydrogen chloride (HCl), sulfuric acid (H_2SO_4), phosphoric acid (H_3PO_4) and nitrous acid (HNO_2) [42]. In this type of pre-treatment, the solubilisation of proteins and carbohydrates present in WAS increases with decreasing pH, as evidenced by Sahinkaya [24]. Devlin et al. [43] concluded that acidification increased COD solubilisation and biogas production. More specifically, a 17 % and 32 % increase was found after 21 days of digestion at pH 2 and 1, respectively. It appears that the more acidic conditions allow doubling the biogas production, although this implies the use of large amounts of acids. Moreover, a subsequent adjustment of the pH to alkaline values is necessary to reach the optimum conditions for anaerobic digestion. Notwithstanding, it is still necessary to purchase reactors that can tolerate acidic conditions, which increases the capital investment costs [4].

Advanced Oxidation Technologies

The most commonly used oxidation processes include hydrogen peroxide, ozone and Fenton's reagents. These pre-treatment technologies rely on the oxidation power of oxidants and in the formation of highly reactive species, such as hydroxyl radicals [4]. The ozonation process is reviewed in more detail hereafter. In pre-treatment by ozonation, the reagent dose is a very important parameter influencing its effectiveness. Goel et al. [44] found that COD solubilisation and methane production increased with increasing ozone dose from 0.015 $gO_3 \cdot (gTS)^{-1}$ to 0.05 $gO_3 \cdot (gTS)^{-1}$. Nevertheless, from a given threshold the methane production and COD solubilization tended to decrease. Silvestre et al. [45] reported that doses above 0.063 $gO_3 \cdot (gTS)^{-1}$ negatively affected biogas production due to mineralisation (conversion of organic matter into CO_2, reducing the amount of carbon available for biogas production). Despite the positive effects of this process on the performance of AD, the production of ozone and the process of transferring it to the sludge is very expensive energetically [22].

2.2.4 Biological Pre-Treatments

Biological pre-treatments are those using aerobic, anaerobic (two-phase digestion), and enzymatic processes. These have shown to be promising in improving the efficiency of hydrolysis in AD. More specifically, several authors have proven their effectiveness in terms of various parameters, such as COD solubilisation, disintegration of the sludge structure and methane production. For instance, Montalvo et al. [46] and Barati Rashvanlou et al. [47] studied a system of air injection into the anaerobic digester and obtained increments up to 200 % in methane production. Moreover, regarding two-phase digestion, Ge et al. [48] concluded that the best results were obtained for the pre-treatment at 65 °C, and pH 6-7 for 1-2 days. The enzymatic process has also shown promising results at adequate enzyme dosages [49, 50]. However, despite being considered environmentally friendly methods, their effectiveness is compromised by high equipment costs (aerobic and anaerobic systems) and high enzyme prices [51].

2.2.5 Concluding Remarks

There is still a long way to go regarding the pre-treatment of WAS in WWTPs. This review shows that many limitations prevent the widespread use of these pre-treatments. The main drawbacks are associated with high energy, equipment, and costs of reactants. Furthermore, finding the optimum operating conditions to balance the pre-treatment efficiency with the formation of undesirable substances is also a challenge. Therefore, the development of novel pre-treatment technologies more energy-efficient and cost-effective must be pursued.

2.3 Raceway Pond Reactors

Raceway reactors have been extensively used for production of microalgae in large-scale. In fact, more than 90 % of these systems use this type of reactor worldwide. This is due to its many advantages, like easy scale-up, low cost, low energy consumption and high productivity rates [52]. Given their innumerable advantages, in recent years this type of reactors has also been studied for the removal of contaminants and secondary effluents disinfection by solar photo-Fenton in WWTPs [53].

The application of this type of reactor has never been evaluated for the pre-treatment of WAS in WWTPs. However, its use is very promising, as it presents several benefits that seem suitable for this application. For example, its configuration provides a large area of solar exposure, which is very advantageous, since it allows the disintegration of the sludge through the effect of ultraviolet radiation, promoting the breakdown of cell membranes and consequent release of the content within, making it more available for the microorganisms in AD. Sludge heating is also favoured by the effect of infrared radiation, even more so if a heat insulation material is implemented over the RPR, promoting a greenhouse effect. On the other hand, physical disintegration is expected to occur due to the shear stresses exerted on the flow. Moreover, the RPRs enable to overcome one of the great disadvantages of the pre-treatments mentioned above, since they generally present a low construction cost and a low energy consumption, being able to treat large quantities of sludge, as they present an easy scale-up. Thus, RPRs enable a combination of effects that facilitate the disintegration of the sludge and consequent increase in the AD hydrolysis efficiency, fostering the production of biogas.

In this sense, the design of these reactors is crucial, since it may interfere with several variables, such as the degree of mixing, and the existence of property gradients, namely temperature, solar penetration, dissolved oxygen concentration, among others. In fact, light penetration is a critical factor, since, ideally, all the fluid elements should be exposed the same amount of time to solar radiation. Thus, the design and operating conditions of the RPRs are essential, affecting both its mass transfer and hydrodynamic behaviour [54].

To optimise the design, some aspects such as the geometry, the configuration of bends and the specific design of the paddlewheel, have to be taken into account. Regarding geometry, there are two aspects to consider, the water depth and the aspect ratio (length to wide ratio). Both are important in determining the mixing at both longitudinal and transverse levels. Concerning aspect ratio, more dead zones, with low-velocity and high-pressure vortices, tend to exist for low values. Meanwhile, for high values, the effect of the walls on the head loss is greater and, consequently, the energy consumption is also more significant. Thus, for large scale reactors, an optimum value of 10 is commonly considered [55]. Regarding the water depth, a volume to surface ratio below 0.2 m is recommendable to enhance the light penetration [54].

Another important aspect to consider is the fluid velocity. Typically, velocities above $0.2\ m \cdot s^{-1}$ are used to prevent sedimentation, low levels of mixing and thermal stratification [56].

Several studies have shown that the installation of baffles improves mixing and reduces dead zones in RPRs. Inostroza et al. [54] studied three different configurations, a traditional, an isle partition and a baffles partition, as shown in Figure 2. The authors found that the traditional configuration had higher velocity gradients and a stagnant region after the first bend. A reduction of dead zones was noticed concerning the isle partition. Although, the flow acceleration in the constriction increased head loss, requiring more mechanical energy. The most interesting configuration is the baffles partition, since it is the one that presented a smaller velocity gradient and a lower dead-volume region. Other authors have also previously demonstrated the suitability of the baffles partition, both in CFD and in real experiments [57, 58].

In most of the raceways already studied, the baffles are semicircles of equal length upstream and downstream of the bend. Nevertheless, Inostroza et al. [54] proposed increasing the length of the deflectors at the end of the bend, which allowed the homogenous distribution of the flow, and the minimization of vortex and energy dissipation in this region.

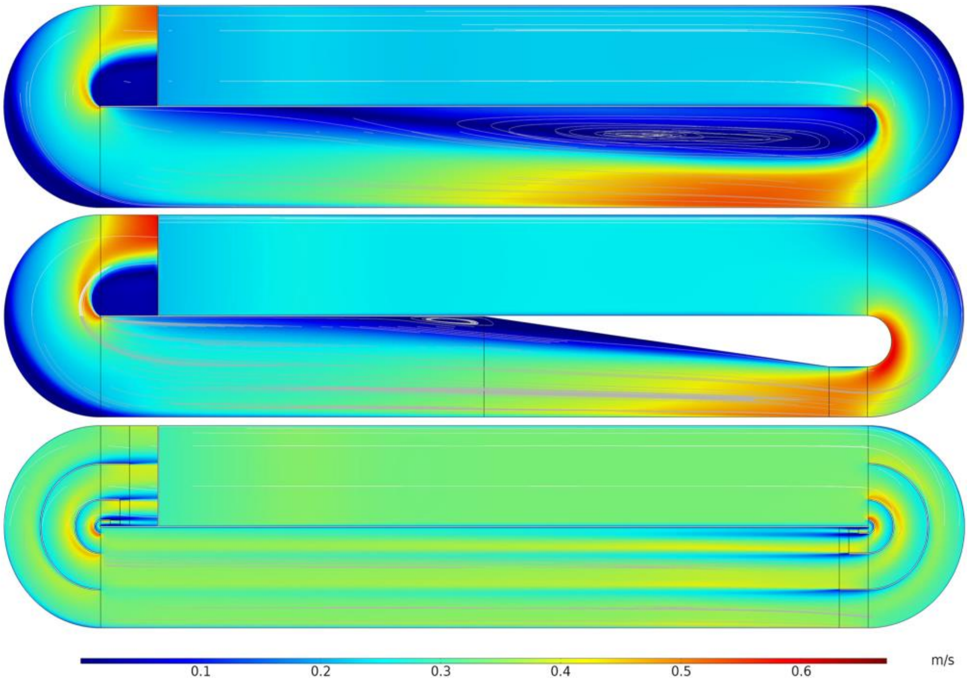

Figure 2. Velocity profiles: Traditional (top), Isle Partition (middle) and Baffles Partition (bottom). Reprinted with permission from Inostroza et al. [54]. Copyright 2021. Elsevier.

In another research, Huang et al. [59] tested the inclusion of sloping baffles at the bottom of the RPR (Figure 3).

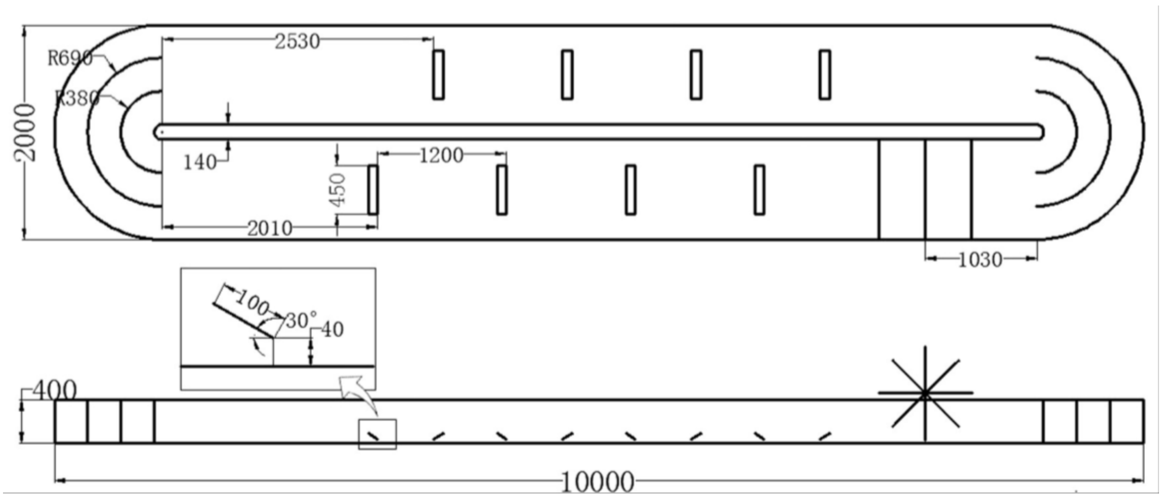

Figure 3. Diagram of the RPR with sloping baffles and flow deflectors. Reprinted with permission from Huang et al. [59]. Copyright 2015. Elsevier.

The authors demonstrated that the sloping baffles combined with the flow deflectors had a higher velocity in the direction of light penetration (depth). This parameter is of great importance, since the higher this velocity, the greater the degree of mixing and the more efficient the utilization of light in the vertical direction. However, the average fluid velocity was reported to be lower due to the resistance imposed by the sloping baffles. Similarly, the percentage of dead zones also increased. These results may limit the application of this type of configurations, so further improvement studies are needed.

Although some studies have already analysed various aspects of the design of RPRs, guidelines covering all its components have never been provided. In this sense, this work proposes design guidelines for this type of reactors, encompassing their global and vertical flow, as well as the specific design of the paddlewheel and its comparison with other fluid circulation systems.

3 Numerical Methods

CFD simulations were performed using the ANSYS 2022 R2 software. The simulations were divided into different 2D subdomains, to avoid the simulation of the 3D domain, reducing the computational resources, making it possible to study more aspects of the RPR and to carry out the work in the pre-established time.

3.1 Governing Equations

The Ansys Fluent flow simulations are all based on conservation laws, i.e., the mass (or continuity) and the momentum (Newton's second law) conservation equations. Energy and species conservation equations should also be considered for flows involving heat transfer or species mixing. Moreover, for turbulent flows, transport equations are additionally solved [60].

Considering the Einstein notation, the mass conservation equation is given by,

$$\frac{\partial \rho}{\partial t} + \frac{\partial}{\partial x_i}(\rho u_i) = 0 \tag{3.1}$$

and the momentum conservation equation by,

$$\frac{\partial}{\partial t}(\rho u_i) + \frac{\partial}{\partial x_j}(\rho u_i u_j) = -\frac{\partial p}{\partial x_i} + \frac{\partial}{\partial x_j}\left[\mu\left(\frac{\partial u_i}{\partial x_j} + \frac{\partial u_j}{\partial x_i} - \frac{2}{3}\delta_{ij}\frac{\partial u_l}{\partial x_l}\right)\right] + \rho g_i + F_i \tag{3.2}$$

where u represents the fluid velocity, ρ is density of the fluid, t is the time, μ is the molecular viscosity, p is the static pressure, δ_{ij} is the Kronecker delta ($\delta_{ij} = 1$ if i=j and $\delta_{ij} = 0$ if $i \neq j$), and $\rho\, g_i$ and F_i correspond to the body forces (gravitational and external, respectively). i, j, and l are indexes, associated with the x, y, and z cartesian components. The indexes i, j, and l can assume any of the x, y, and z directions. For incompressible flows, the first term of the continuity equation is considered null [60].

In this work, the energy equation was not solved since the flow is isothermal.

3.1.1 RANS Equations

Given the characteristics of the flow and the imposed boundary conditions, the flow is considered turbulent. Thus, it is useful to introduce the principles of time averaging due to the random nature of turbulent fluctuations. The most common approach used for computing turbulent flow is the Reynolds Average Navier-Stokes (RANS). In this method, the equations are decomposed into the mean and fluctuating components. For the velocity it translates into $u = \bar{u} + u'$, where $\bar{u}$ and u' correspond to the mean and fluctuating velocity components, respectively. For other scalar quantities, like energy, species concentration, and pressure it is described for $\varphi = \bar{\varphi} + \varphi'$. Thus, these variables now represent time-averaged values [60]. The continuity equation takes the same form as above in Equation 3.1. The momentum RANS equation is described by

$$\frac{\partial}{\partial t}(\rho u_i) + \frac{\partial}{\partial x_j}(\rho u_i u_j) = -\frac{\partial p}{\partial x_i} + \frac{\partial}{\partial x_j}\left[\mu\left(\frac{\partial u_i}{\partial x_j} + \frac{\partial u_j}{\partial x_i} - \frac{2}{3}\delta_{ij}\frac{\partial u_l}{\partial x_l}\right)\right] + \frac{\partial}{\partial x_j}\left(-\rho\overline{u_i' u_j'}\right) \quad (3.3)$$

As a result of interactions between various turbulent fluctuations, additional terms appear in the ensemble-averaged flow equations. These non-linear Reynolds stress terms require modelling using classical turbulence models to close the system of mean flow equations [60].

In 1877, Boussinesq suggested that these Reynolds stresses, τ_{ij}, also known as turbulent shear stresses are proportional to mean rates of deformation [60], as follows

$$\tau_{ij} = -\rho\overline{u_i' u_j'} = 2\mu_t S_{ij} - \frac{2}{3}\rho k\delta_{ij} \quad (3.4)$$

where μ_t represents the turbulent or eddy viscosity and S_{ij} the mean strain rate tensor.

Several turbulence models can describe flow hydraulics. In this work, the standard k-ε, k-ε RNG and k-ω SST models were assessed. After an analysis, it was concluded that the standard k-ε model is the best suited for the raceway reactor, describing the flow hydrodynamics more accurately, which agrees with the available data in the literature [54, 58].

3.1.2 Standard k-ε model

The Standard k-ε model is characterised by being robust, economical, and reasonably accurate for a wide variety of turbulent flows, which makes it extensively used and popular in heat transfer and industrial flow simulations. It is a semi-empirical model and is based on transport equations for the turbulent kinetic energy, k, and the turbulent dissipation rate, ε [60].

Considering valid to assume that the flow is fully turbulent, the turbulent kinetic energy and its dissipation rate are calculated respectively from

$$\frac{\partial}{\partial t}(\rho k) + \frac{\partial}{\partial x_i}(\rho k u_i) = \frac{\partial}{\partial x_j}\left[\left(\mu + \frac{\mu_t}{\sigma_k}\right)\frac{\partial k}{\partial x_j}\right] + G_k + G_b - \rho\varepsilon - Y_M + S_k \quad (3.5)$$

$$\frac{\partial}{\partial t}(\rho\varepsilon) + \frac{\partial}{\partial x_i}(\rho\varepsilon u_i) = \frac{\partial}{\partial x_j}\left[\left(\mu + \frac{\mu_t}{\sigma_\varepsilon}\right)\frac{\partial\varepsilon}{\partial x_j}\right] + C_{1\varepsilon}\frac{\varepsilon}{k}(G_k + C_{3\varepsilon}G_b) - C_{2\varepsilon}\rho\frac{\varepsilon^2}{k} + S_\varepsilon \quad (3.6)$$

where G_k corresponds to the generation of turbulent kinetic energy because of the mean velocity gradients. G_b is the generation of turbulence kinetic energy owing to buoyancy. Y_M corresponds to the contribution of the fluctuating dilation in compressible turbulence to the overall dissipation rate. σ_k and σ_ε are the turbulent Prandtl numbers for k and ε, having default values of 1.0 and 1.3, respectively. $C_{1\varepsilon}$, $C_{2\varepsilon}$, $C_{3\varepsilon}$ are constants. $C_{1\varepsilon}$ and $C_{2\varepsilon}$ have default values of 1.42 and 1.68, respectively [60]. S_k and S_ε are user-defined terms, which are not used in this work.

The turbulent viscosity, μ_t is computed as follows,

$$\mu_t = \rho C_\mu \frac{k^2}{\varepsilon} \tag{3.7}$$

where C_μ has a default value of 0.09.

3.1.3 Transport equation

The performance of a tracer injection to study the vertical mixing in the reactor requires the activation of species transport equation.

The chemical species conservation equation is a convection-diffusion equation, through which the local mass fraction, Y_n, of each specie n^{th} can be predicted. It can be given by,

$$\frac{\partial}{\partial t}(\rho Y_n) + \frac{\partial}{\partial x_i}(\rho u_i Y_n) = -\frac{\partial J_n}{\partial x_i} + R_n + S_n \tag{3.8}$$

in which R_n is the rate of formation of species n by chemical reaction, and S_n represents any user-defined sources. The two last terms of the right-hand side were not considered in this work since there are no chemical reactions and source terms were not added. J_n is the diffusion flux of a certain species n that, for turbulent flows, can be calculated by,

$$J_n = -\left(\rho D_{n,m} + \frac{\mu_t}{\mathrm{Sc_t}}\right)\frac{\partial Y_n}{\partial x_i} + \rho D_{T,n}\frac{1}{T}\frac{\partial T}{\partial x_i} \tag{3.9}$$

in which μ_t is the turbulent viscosity, $D_{n,m}$ is the mass diffusion coefficient, T is the temperature, $D_{T,n}$ is the Soret diffusion coefficient, and $\mathrm{Sc_t}$ is the Schmidt number ($\frac{\mu_t}{\rho D_t}$, where D_t is the turbulent diffusivity) that has a default value of 0.7 [60]. This equation's last term is deemed null as the flow is isothermal.

3.1.4 Discrete Phase Model

The Discrete Phase Model (DPM) with discrete random walk was used to simulate the behaviour of discrete particles in the RPR. The ANSYS Fluent software follows the Euler- Lagrange approach to simulate the discrete Lagrangian model. In this case, water is the fluid phase, and the particles constitute the dispersed phase. The particle-particle interactions were neglected.

The ANSYS Fluent calculates the path of an individual particle by considering the balance of forces acting on it. This calculation is done using a Lagrangian reference frame, where the forces acting on the particle are equated to its inertia [60], as follows

$$m_p\frac{\partial u_p}{\partial t} = m_p\frac{u - u_p}{\tau_r} + g\frac{\rho_p - \rho}{\rho_p} + F \tag{3.10}$$

in which m_p is the particle mass, u is velocity of the fluid phase, u_p is velocity of the particle, ρ_p is the density of the particle, F is an additional force, $m_p\frac{u-u_p}{\tau_r}$ is the drag force, and τ_r is the particle relaxation time determined by

$$\tau_r = \frac{\rho_p d_p^2}{18\mu} \frac{24}{C_D Re_r} \tag{3.11}$$

where d_p is the diameter of the particle and $\mathrm{Re_r}$ is the relative Reynolds number, computed as

$$\mathrm{Re_r} = \rho \frac{d_p |u_p - u|}{\mu} \tag{3.12}$$

In this work the additional forces, F , and the rotation of the particles were neglected.

A stochastic tracking model can be used to predict the particles dispersion caused by turbulence in the fluid phase. This model incorporates the influence of instantaneous turbulent velocity fluctuations on the trajectories of particles by employing stochastic methods. ANSYS Fluent utilises the Discrete Random Walk (DRW) model as a specific stochastic approach, in which the fluctuating velocity components can be described as discrete piecewise constant functions of time. The random values associated with these components remain constant over a specific time interval determined by the characteristic lifetime of the turbulent eddies [60].

Therefore, the prediction of the dispersion of the particles due to the turbulence requires the inclusion of the instantaneous value of the fluctuating fluid velocity in Equation 3.10, such that $u = \bar{u} + u'$. In addition, it should be considered that the DRW model presupposes that the values of u' can be described by a Gaussian probability distribution [60] so that,

$$u' = \zeta \sqrt{\overline{u'^2}} \tag{3.13}$$

in which ζ is a normally distributed random number and $\sqrt{\overline{u'^2}}$ can be described (assuming isotropy) by,

$$\sqrt{\overline{u'^2}} = \sqrt{2k/3} \tag{3.14}$$

3.1.5 VOF Model

There are two approaches to characterize multiphase flows: the Euler-Euler and the Euler-Lagrange approach. In the first, the distinct phases are treated as a continuum and, as such, it uses continuous transport equations for each phase. On the other hand, in the second approach one phase is considered continuous and the other disperse. Thus, it can be used when the discrete phase occupies a small fraction of the volume, so it can be neglected [60].

The Euler-Lagrange approach is inadequate for this work since both phases occupy considerable volume fractions. Regarding the Euler-Euler approach, ANSYS Fluent has three available models: the Eulerian, volume of fluid (VOF), and mixture models. The VOF model was selected in the present work since it is the most suitable to represent free-surface flows, where a well-defined interface exists. In this model, only one set of momentum equations is solved, and the volume fraction of both fluids is tracked throughout the domain.

There are a liquid and a gas phase for this case, so the equations will only include these two terms. The continuity equation (Equation 3.1) is solved considering a volume-fraction-averaged mixture density, ρ, calculated by,

$$\rho = \alpha_L \rho_L + \alpha_G \rho_G \tag{3.15}$$

where ρ_L and ρ_G are the density of the liquid and gas phases, and α_L and α_G are the volume fractions of the liquid and gas phases, respectively. Both phases' volume fraction must be between 0 and 1. Accordingly, the sum of the liquid and gas phases volume fraction in each cell must be equal to 1. This restriction implies that the volume fraction equation only needs to be solved for the secondary phase as the other can be determined by difference. Thus, considering the gas as the primary phase, the liquid volume fraction can be calculated by,

$$\frac{\partial}{\partial t}(\alpha_L \rho_L) + \frac{\partial}{\partial x_i}(\alpha_L \rho_L u_{L,i}) = \dot{m}_{GL} - \dot{m}_{LG} \tag{3.16}$$

where $\dot{m}_{GL}$ is the mass transfer from the gas phase to the liquid phase and $\dot{m}_{LG}$ is the mass transfer from the liquid phase to the gas phase.

Concerning the momentum conservation equation, described in Equation 3.3, the difference is related to the way how μ is defined. So μ corresponds to the volume-fraction-averaged dynamic viscosity and can be given by,

$$\mu = \alpha_L \mu_L + \alpha_G \mu_G \tag{3.17}$$

in which μ_L and μ_G represent the dynamic viscosities of the liquid and gas phases, respectively.

The gravity forces were considered for the implementation of the VOF model and the gravitational acceleration fields were set. In addition, the open channel flow option was activated. This approach enables the characterization of flows involving a free surface located at the interface between the moving phase and the phase above it (typically the atmosphere).

The dimensionless Froude number allows to describe open channel flows. It enables the characterization of the flow as subcritical, critical or supercritical depending if its value is inferior, equal or superior to 1, respectively. This definition is related to whether or not downstream conditions affect upstream flow. Thus, the Froude number is described as the ratio between inertia and hydrostatic forces [60],

$$Fr = u/\sqrt{g y_b} \tag{3.18}$$

where u is the velocity magnitude and y_b is the distance from the bottom to the free-surface.

4 Overall Flow Design

The first part of the work comprised the study on the xy plane of the raceway reactor hydrodynamics, and the impact of the implementation of flow deflectors on it.

4.1 CFD Model

4.1.1 Geometry

The computational domain geometry consists of an open channel with a bend where the fluid reverses the flow direction. It was constructed using Design Modeler, one of the CAD modules available in Ansys Workbench 2022 R2. The 2D configuration represents the top view of the raceway. It should be noted that only half of the reactor has been considered, as there is a symmetry at the *inlet/outlet* plan, as shown in Figure 4. The boundaries were defined as *inlet*, *outlet*, *innerwalls*, and *outerwalls*, while the rest of the domain was set as fluid. Figure 4 shows a sketch of the geometry considered. The CFD domain is described as L_{in} = 1 m, L_{out} = 1 m, L_{w} = 10 m, L_{m} = 0.15 m, and R = 1 m.

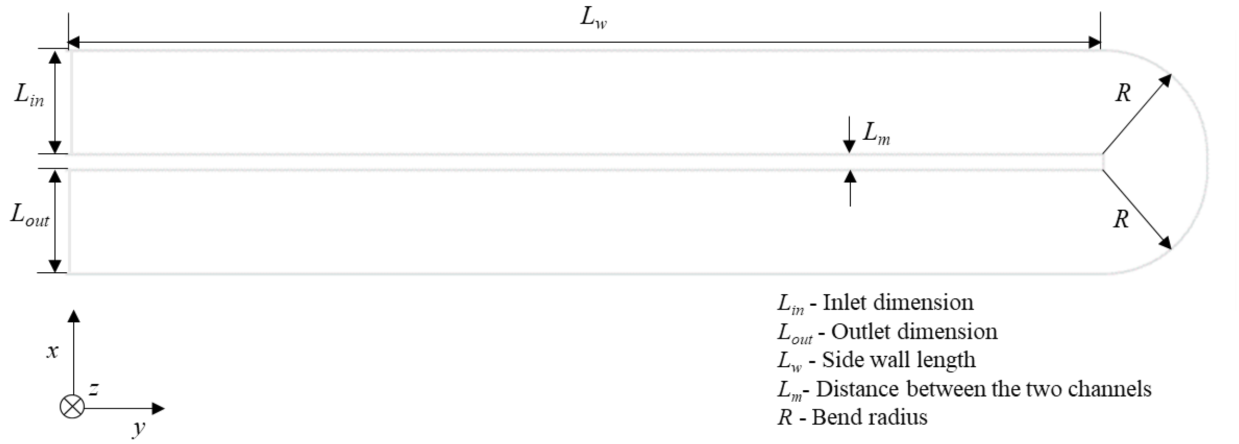

Figure 4. Geometry of the 2D domain.

The simulated reactor has the dimensions of a real-scale RPR, having a total surface area of 43.4 m^2. In this work, the configuration of flow deflectors on the RPR curve was studied aiming to improve the overall flow distribution after the U-turn. The position and distance of these baffles to the wall were also a factor of analysis.

4.1.2 Boundary and Initial Conditions

For CFD solution, boundary and initial conditions need to be defined. The governing equations, described previously in Section 3.1, must be integrated since partial derivative equations mainly constitute them. In this sense, boundary conditions must be defined, being an essential mathematical model component.

The boundary conditions must be set at the walls and regions where the fluid enters or leaves the domain (inlet and outlet channels). There may also be symmetry, periodic or axis boundaries in some cases.

In the present work, the working fluid was set as water at 20 °C, ρ = 998.2 kg·m^{-3} and μ = 1.003 mPa·s. Concerning the inlet boundary condition, the velocity was defined at 0.3 m·s^{-1}. Furthermore, a turbulence intensity of 5 % and a turbulent viscosity ratio of 10 were set.

The near-wall treatment significantly influences the numerical simulations' results since walls substantially affect the flow turbulence and vorticity. Several wall functions were tested, including Standard, Scalable, Non-equilibrium and Enhanced Wall Treatment. The Scalable wall functions were chosen, since the y^+ values did not remain in the log-law region, i.e., in the totally turbulent layer (30 < y^+ < 300), which render the use of Standard and Non-Equilibrium wall functions unappropriated. Moreover, the use of Enhanced Wall Treatment, which is a y^+-insensitive wall treatment, became impractical since the solution did not converge. Thus, the Scalable wall functions seemed to be the most appropriate, as they avoid the inaccurate modelling of the laminar and buffer region of the boundary layer, making the near-wall mesh point present a value of y^*=11.225, regardless of how close it is to the wall.

A no-slip condition was established at the walls, which imposes the velocity components x and y to zero. At the outlet channel, a constant gauge pressure (pressure relative to the atmospheric pressure) of 0 Pa was defined.

4.1.3 Models and Solution Methods

For all the CFD simulations, a pressure-based solver was used. Coupled scheme was used for the Pressure-Velocity Coupling. Concerning the Spatial discretization, Least Squares Cell Based was chosen for the gradient; Second Order for the pressure; Second Order Upwind for the Momentum; and First Order Upwind for the Turbulent Kinetic Energy and for the Turbulent Dissipation Rate. Regarding the overall flow design, the simulations were performed at steady state, i.e., the transient terms were set to zero. The residuals for all the equations were defined at 10^{-6}.

4.1.4 Mesh

The grid independence test is crucial to study the dependence of the results on the mesh refinement. In general, the finer the element size, the more accurate the numerical results and the more time-consuming the CFD simulations. Thus, a trade-off between the accuracy of the results and the computation time has to be made.

All the meshes tested were generated using Meshing, one of the modules available in Ansys 2022 R2 for generating meshes from a CAD model and using the default quadrilateral dominant method. The presence of walls implies the existence of boundary layers, where large gradients (velocity, pressure, etc.) exist, especially in turbulent flows. Therefore, using very fine meshes close to the walls becomes necessary to solve these gradients properly. Thus, inflation with 10 layers and 1.2 growth rate was applied for every wall surface.

4.2 Results

4.2.1 Mesh Independence Test

Five meshes with different number of elements were tested. The mesh was validated using as parameters the streamlines, the turbulent kinetic energy, the turbulent dissipation rate, the head loss between the inlet and the outlet, and the wall shear stresses. Table 1 shows the element size and the number of elements for each mesh studied.

Table 1. Element sizes and number of elements for each mesh studied.

	Mesh05	Mesh03	Mesh025	Mesh02	Mesh018
Element size /m	0.05	0.03	0.025	0.02	0.018
Number of elements	16192	37069	50034	73425	88836

Figures 5, 6 and 7 show the streamlines, the turbulent kinetic energy, k, and the turbulent dissipation rate, ε, in the raceway reactor. These maps enable to assess the flow dependence on the grid used.

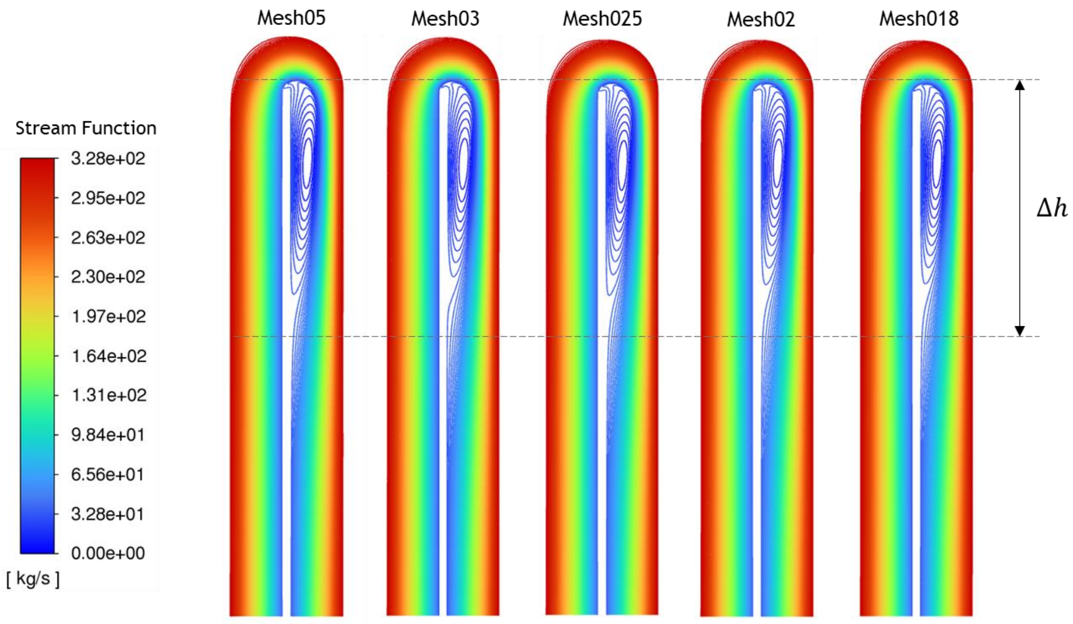

Figure 5. Flowrate streamlines of meshes 05, 03, 025, 02 and 018.

Streamlines contours in Figure 5 show that there are no relevant differences between the different meshes. After the flow reversal, all present a large recirculation zone near the inner wall. The length of this recirculation zone, Δh, is practically equal for all meshes, as Figure 5 shows. These areas, where the density of streamlines is lower, are characterized as dead zones, i.e., regions where the fluid velocity is reduced, so it remains stagnant for a long time.

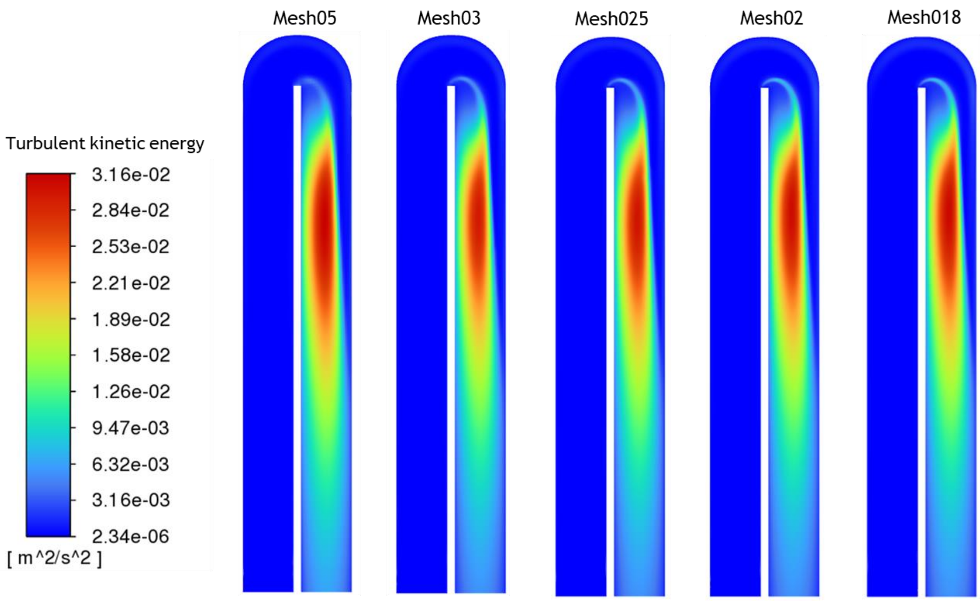

Figure 6. Turbulent kinetic energy, k, of meshes 05, 03, 025, 02 and 018.

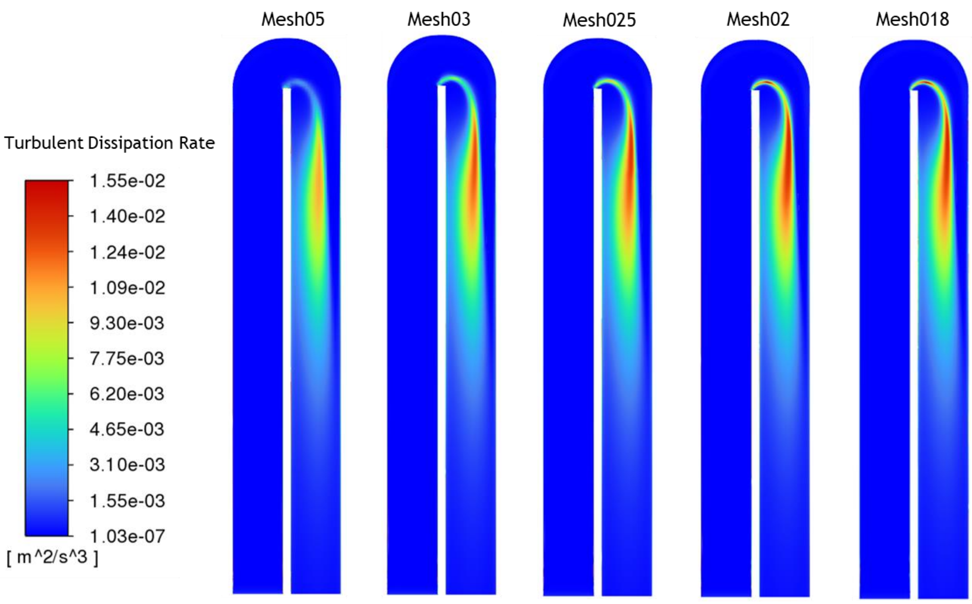

Figure 7. Turbulent dissipation rate, ε, of meshes 05, 03, 025, 02 and 018.

Figure 6 shows that the turbulent kinetic energy is concentrated in the region after the flow inversion, being dissipated along the channel. This may be attributed to the abrupt change in the direction of flow. This region also coincides with the area of the largest turbulent dissipation rate (Figure 7). This results from the interaction between eddies that cause turbulent dissipation of the flow momentum [61]. Moreover, it can be noted that from Mesh025 onwards, the contour maps are very similar, showing uniformity in the characterization of the turbulent flow. However, this analysis is subjective, since it depends on the visual perception of the image. Therefore, in order to make a more detailed and accurate study, the total pressure difference in the flow and the shear stresses on the wall were calculated. Table 2 and Figure 8 show the results obtained for each mesh tested.

Table 2. Total pressure difference, Δp, and wall shear stresses, τ, for each mesh studied.

	Mesh05	Mesh03	Mesh025	Mesh02	Mesh018
Δp/Pa	111.2	114.3	116.0	117.7	118.4
τ/N	11.5	12.0	12.5	13.2	13.6

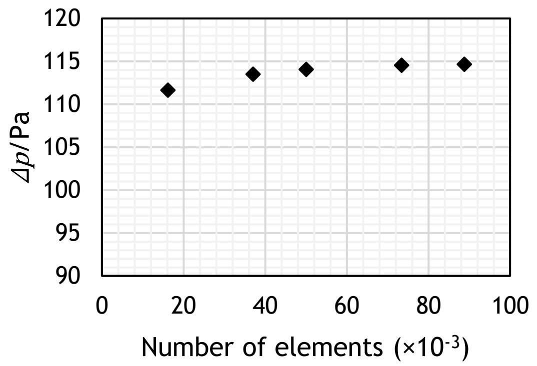

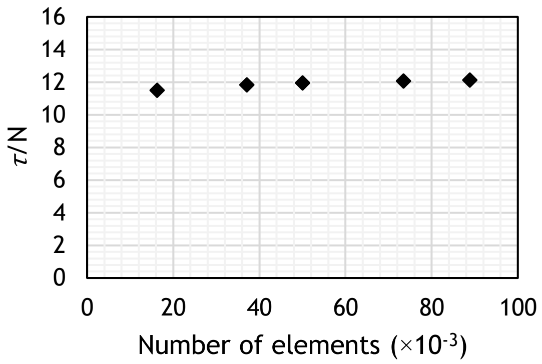

Figure 8. Total pressure difference, Δp, and wall shear stresses, τ, for each mesh studied.

Results show that Mesh02 is the most appropriate since it presents an error relative to the most refined mesh lower than 2 % regarding Δp and an error smaller than 1 % regarding τ. This mesh is preferable to Mesh018 since it enables reducing the simulation time and computational resources. Thus, Mesh02 presents the best trade-off between the accuracy of the results and the time expended for simulations. Figure 9 shows some of the details of the chosen mesh, i.e., Mesh02. It shows the different zones of the raceway reactor, including cell geometry and wall inflation.

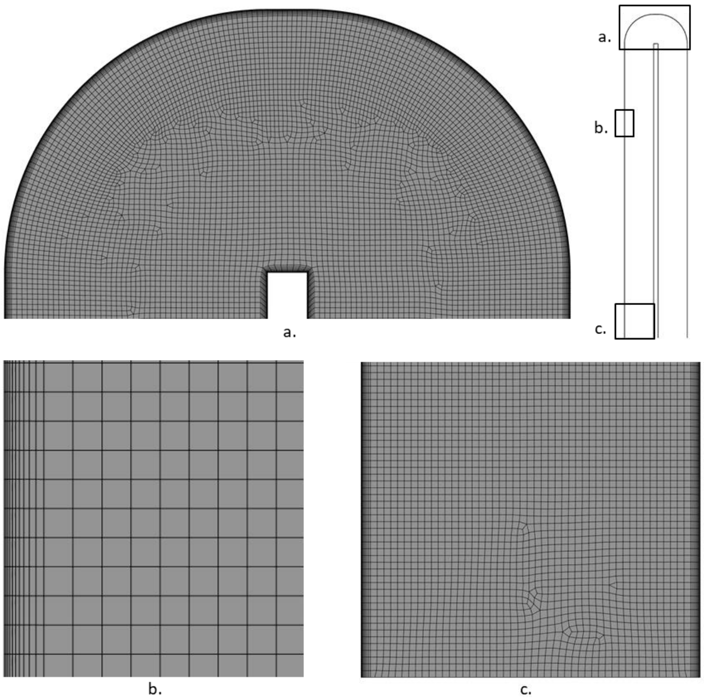

Figure 9. Mesh02 details for different zones.

4.2.2 RPR Flow Deflectors Design

The setup of flow deflectors on the reactor U-turn was investigated to improve the flow distribution and reduce the recirculation zones. These were installed according to the configuration shown in Figure 10. Initially, the values of x_1, x_2, L_1 and L_2 were defined as 0.27 m, 0.68 m, 0.6 m, and 0.6 m, respectively. Subsequently, different values of these parameters were analysed to optimise the geometry.

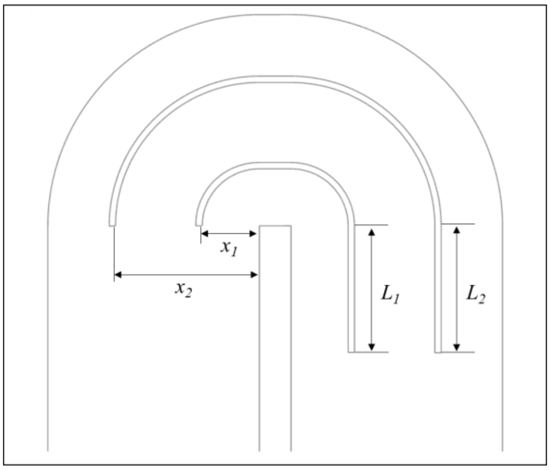

Figure 10. Flow deflectors 2D geometry.

The mesh was validated using the same methodology described in Section 4.2.1. In this case, inflation was also applied to the baffles' walls using 10 layers and a growth rate of 1.2.

Table 3 shows the number of elements, the element size, the total pressure difference, Δp, and the wall shear stresses, τ, for each mesh studied.

Table 3. Element size, number of elements, Δp and τ for each mesh evaluated.

	Mesh05	Mesh03	Mesh025	Mesh02	Mesh018
Element size /m	0.05	0.03	0.025	0.02	0.018
Number of elements	17778	39361	52833	76984	92431
Δp/Pa	37.4	35.3	34.8	28.6	28.4
τ/N	10.0	10.1	10.1	9.9	9.9

Once again, Mesh02 was chosen since the quality of the results is good enough, presenting an error lower than 1 % regarding both the Δp and τ, and the simulation time is not too long. Figure 11 shows the mesh details in the vicinity of the baffles, where inflation in their walls can be observed.

As previously mentioned, different geometries of the deflectors in the reactor were tested. The different values considered for parameters x_1, x_2, L_1, and L_2 (Figure 10) are presented in Table 4. The streamline maps were compared before and after the implementation of the flow deflectors, and for the different configurations to assess the influence of the baffles' installation. Figure 12 shows these contours, focusing on the raceway area where this difference is remarkable. In addition, the outlet's velocity profile was also compared to assess this parameter's uniformity. The corresponding graph is presented in Figure 13. The case identified as ND corresponds to the configuration with no deflectors.

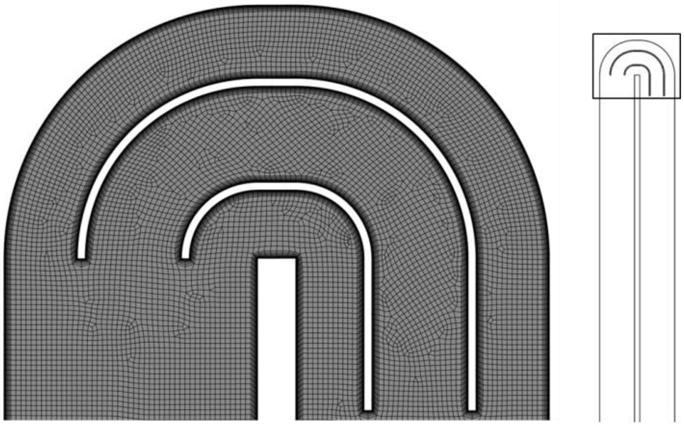

Figure 11. Mesh details for flow deflectors zone.

Table 4. Values of x_1, x_2, L_1 and L_2 for each design point analysed.

Design Point	x_1/m	x_2/m	L_1/m	L_2/m
dp0	0.27	0.68	0.6	0.6
dp1	0.27	0.68	0	0
dp2	0.27	0.68	0.5	0.7
dp3	0.3	0.71	0.5	0.7
dp4	0.33	0.74	0.5	0.7
dp5	0.42	0.78	0.5	0.7

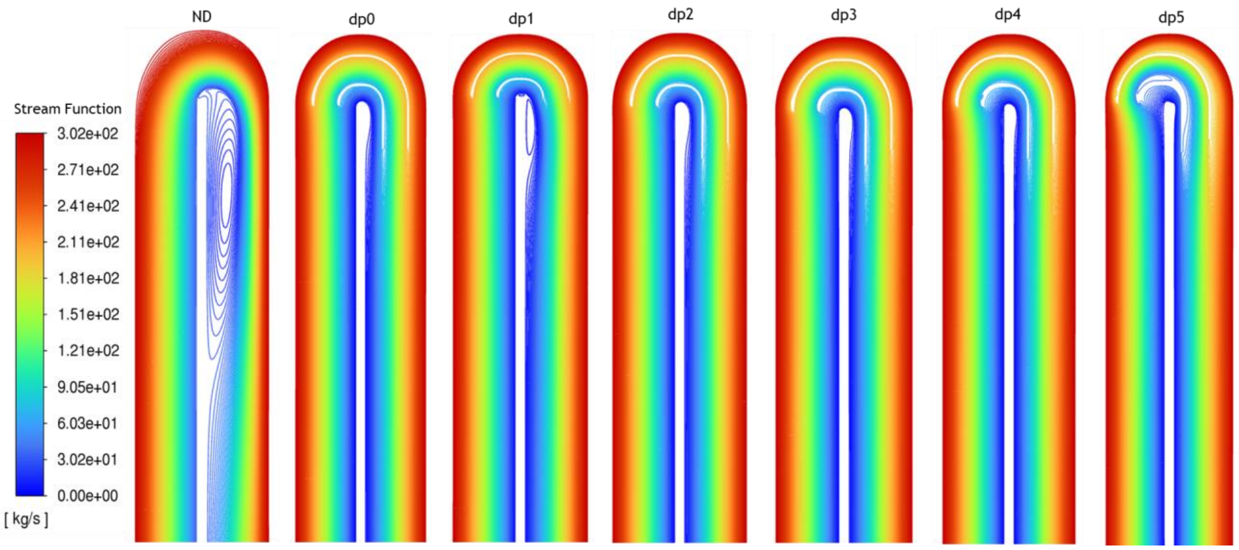

Figure 12. Flowrate streamlines before, ND, and after the implementation of flow deflectors for the different configurations studied.

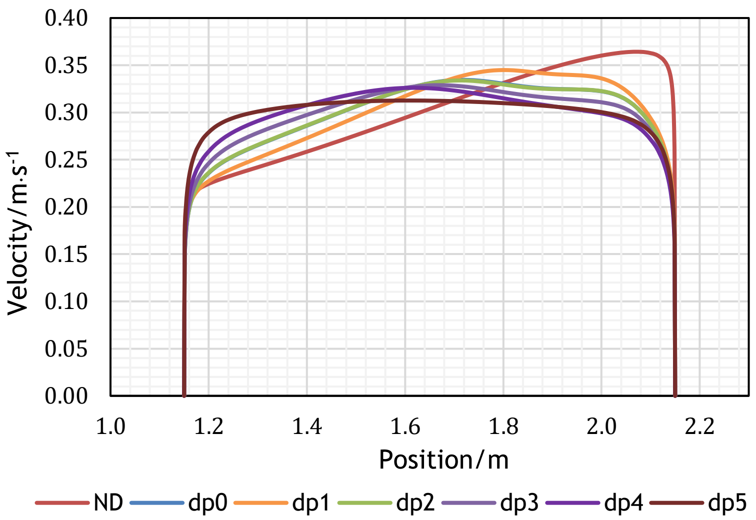

Figure 13. Velocity profiles at the outlet for the different RPR deflectors configurations.

Figure 12 shows a clear reduction in the recirculation zones after the inclusion of the flow deflectors, which results in a more uniform and stable flow, as can be proven by the velocity profiles in Figure 13. As demonstrated by other authors, comparing cases dp0 and dp1, it turns out that the extension of the deflectors at the end of the raceway curve helps to distribute the flow uniformly, minimizing the creation of vortices and energy dissipation at this location. Moreover, comparing cases dp0 and dp2, where the difference is related to lengths L_1 and L_2, the case where the length of the baffle near the inner wall is greater presents a slightly more uniform velocity at the outlet. Thus, it was concluded that this configuration would be preferable. However, it turns out that the velocity at the outlet is higher on the side of the outer wall. Therefore, it was stipulated that the baffles could be moved to the left.

Cases dp3, dp4 and dp5 show a progressive leftward movement of the baffles. This modification makes the velocity at the outlet much more uniform, resulting in a fairly flat velocity distribution for dp5. Nonetheless, additional stagnant areas are generated near the baffles, which may cause the accumulation of deposits and sedimentation in these regions. These would have to be removed, resulting in additional costs and operation interruption. It was accordingly decided that the best case would be dp2, since the difference in the velocity profiles at the outlet observed in cases dp3, dp4, and dp5 does not outweigh the appearance of stagnant fluid zones. Additionally, this case presents an easier construction and scale-up, as the flow deflectors are centered and have a symmetric U-turn.

To assess the efficiency of the implementation of flow deflectors, another very important factor to consider is the pressure drop along the reactor. In these flows, most of the head losses occur in the raceway bend. This happens due to the boundary layer separation phenomenon, i.e., due to the abrupt change in the direction of the fluid velocity [62]. The implementation of deflectors is a solution that minimises this effect. After the baffles set up the head losses are considerably reduced, from about 118 Pa (Table 2) to 29 Pa (Table 3). Therefore, the mechanical energy consumption will be much lower, as it is directly proportional to the head loss in the RPR.

5 Vertical Flow

In the second part of this work, a representative subdomain of the reactor depth on the yz plane was analysed, pretending to study the vertical mixing on it.

5.1 CFD Model

5.1.1 Geometry and Mesh

The computational domain geometry consists of a rectangular section of the raceway axial plan aligned with the flow direction and normal to the top-view plan, as shown in Figure 14. A length, L, of 1 m and a height, h, equivalent to the reactor sludge level, of 0.1 m were considered. The blue zones represent periodic boundary conditions, described further in Section 5.1.2.

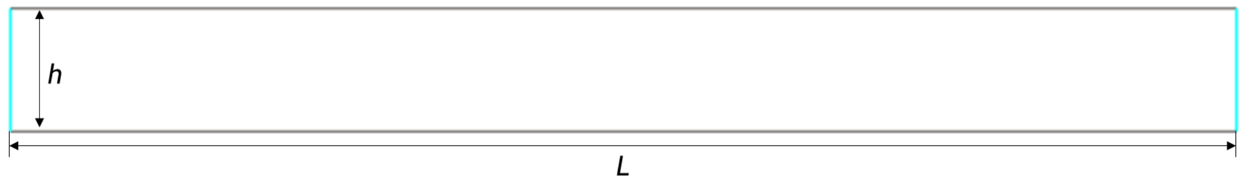

Figure 14. RRP Depth Plan 2D Geometry.

The mesh was refined using the same method described in Section 4.2.1, i.e., the quadrilateral dominant method. At the bottom wall, inflation with 10 layers and a growth rate of 1.2 were defined. The mesh independence test is described in Appendix A, as it is similar to the performed in Section 4.2.1. A final grid with an element size of 0.005 m and 5800 elements was obtained.

5.1.2 Boundary Conditions

Regarding the boundary conditions, at the bottom wall, a no-slip condition was established. At the top, shear stress equal to zero was specified, considering the top as a free surface exposed to the atmosphere.

Periodic boundary conditions (PBCs) at the left and right-hand sides were implemented to take advantage of the repeating nature of the flow. For that purpose, it was necessary to estimate the pressure drop value per unit length, $\Delta p/L$. Then, Manning's equation was applied. This empirical equation relates the velocity in an open channel with its geometry, slope, and coefficient of friction. It can be described by,

$$u = \frac{k_n}{n_r} R_h^{\frac{2}{3}} S^{\frac{1}{2}} \tag{5.1}$$

where u is the cross-sectional fluid velocity in $m \cdot s^{-1}$; k_n is a constant (1.0 for SI units); n_r is the Manning coefficient of roughness, ranging from 0.01 (for a smooth and clean surface) to 0.06; R_h is the hydraulic radius in m, and S represents the slope in $m \cdot m^{-1}$ [63].

For channels with a width-depth ratio greater than or equal to 10, the mean depth can replace the hydraulic radius, and so $R_h = h$. Thus, assuming an average velocity of 0.3 $m \cdot s^{-1}$, and a totally smooth channel made of, for example, polyvinyl chloride, $n_r = 0.01$, it was estimated an S value of 1.94×10^{-4} $m \cdot m^{-1}$.

Finally, the $\Delta p/L$ value was determined according to

$$\frac{\Delta p}{L} = S\rho g \tag{5.2}$$

where g is the acceleration of gravity, 9.8 $m \cdot s^{-2}$.

5.1.3 Solution Methods

The methods referred in Section 4.1.3 were also implemented in this simulation. The species transport was activated for this case since a tracer experiment was carried out. For that purpose, transient simulations were performed. Regarding the transient formulation, the second order implicit method was chosen.

To compute the simulations in transient state, a time-step size, Δt, and the number of time steps, N, were defined. Accordingly, the Courant-Friedrichs-Lewy (CFL) condition was used,

$$\mathrm{Co} = \frac{u_{max}\Delta t}{\Delta x} \tag{5.3}$$

where Co is the Courant number, which represents the number of meshes that the fluid travels during one time-step and assumes a value between 0 and 1 (in this case 0.5); Δx is the mesh element size, and u_{max} is the maximum fluid velocity.

The number of time steps was determined considering simulations of 5 residence times, which can be written as

$$N = \frac{5\,\tau_p}{\Delta t} = \frac{5}{\Delta t}\frac{V}{q} \tag{5.4}$$

in which τ_p corresponds to the residence time, V represents the volume of the geometry domain and q the volume flowrate.

5.2 Results

5.2.1 Rugosity and Δp Assessment

Since understanding the dependence of the flow on the wall's rugosity is of great importance, as it may affect the flow hydrodynamics, the experiments were performed in RPRs using different rugosities at the walls. Thus, a study was carried out pretending to analyse the influence of the roughness height and roughness constant parameters, given in ANSYS Fluent, in the average velocity at the PBCs surface.

Figure 15 shows the variation of the average velocity with roughness height for different roughness constant. The surface is considered totally smooth for a roughness height of 0 and a roughness constant of 0.5. It should be noted that the roughness constant has a maximum value of 1.

As expected, increasing the rugosity decreases the average velocity for the same slope or Δp. As a result, the pressure drop along the reactor becomes significantly greater, meaning more power must be supplied to achieve the same velocity. Therefore, materials with smooth surfaces, that is, minimal roughness, should be preferred wherever possible.

In addition, a comparative study between the velocity determined by the Manning's equation and the velocity determined in the ANSYS Fluent software was made, being presented in Appendix B.

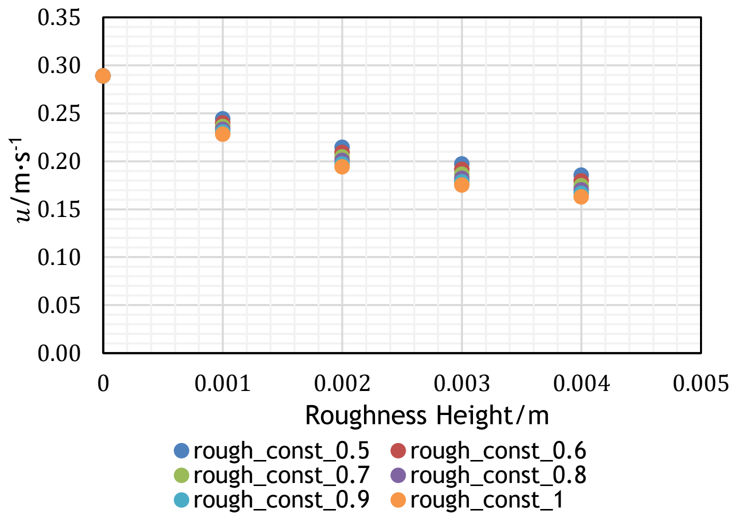

Figure 15. Average velocity dependence on roughness constant and roughness height.

5.2.2 Turbulence Distribution

Turbulence is a complex phenomenon, having various characteristics that may seem highly unpredictable, as it is characterised by unsteady and irregular motion in which transported quantities fluctuate in time and space. To analyse the turbulence distribution in the flow, the turbulent kinetic energy and the turbulent dissipation rate maps were plotted. These are represented in Figures 16 and 17, respectively.

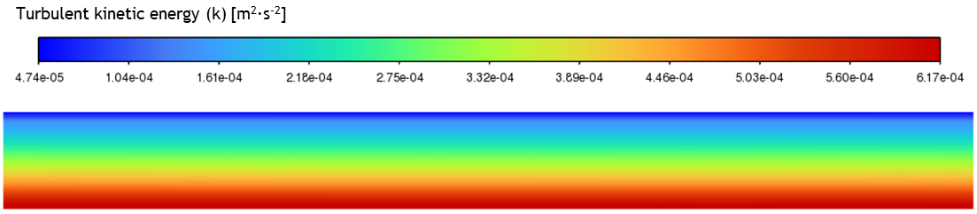

Figure 16. Map of turbulent kinetic energy.

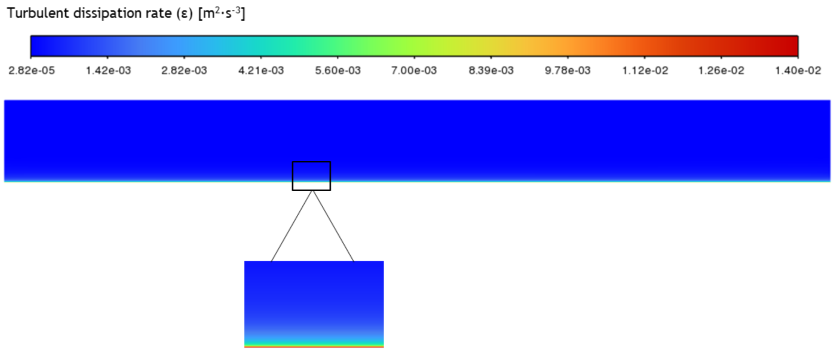

Figure 17. Map of turbulent energy dissipation rate.

According to Figure 16, one can conclude that the turbulent kinetic energy, i.e., the energy contained in the turbulent fluctuations of the fluid flow, is mainly concentrated near the bottom wall of the reactor. This energy is transferred from larger eddies to smaller eddies in a cascade effect. At the so-called Kolmogorov small scales, this energy cascade stops due to the ability of viscous forces to balance inertial forces and dissipate turbulent energy converting it into thermal energy or heat. This dissipation occurs mainly at the bottom wall, where the smallest scales dominate. Accordingly, the close-up in Figure 17 shows a steep gradient of the turbulent energy dissipation rate near the rugous wall, where the transition between eddies of different scales dominates.

5.2.3 Vertical Mixing

The degree of vertical mixing in the flow is an extremely important factor. All the fluid elements should ideally be in each section of the raceway height for the same amount of time. This avoids gradients and ensures a homogeneous exposition of the sludge elements to solar radiation.

For that analysis, some preliminary definitions are required first. The turbulent kinetic energy is described as,

$$k = \frac{1}{2}\left(\overline{u'^2} + \overline{v'^2} + \overline{w'^2}\right) \tag{5.5}$$

where $\overline{u'}$, $\overline{v'}$, and $\overline{w'}$ are the velocity fluctuating components in the cartesian x, y, and z directions, respectively.

As the turbulent kinetic energy is determined from the k-ε simulations, in 2D the fluctuating component of the velocity in the z direction, $\overline{w'}$, is considered null, and $\overline{u'} = \overline{v'}$ for the standard k-ε turbulence model, it was possible to determine the value of the velocity fluctuating component in the y direction, $\overline{v'}$. For this case, $\overline{v'} = 1.84 \times 10^{-2}$ m·s^{-1}.

Since h = 0.1 m, it becomes possible to assess the average time it takes for a fluid element to travel through the vertical section of the reactor, $\tau_{vertical}$,

$$\tau_{vertical} = \frac{h}{\overline{v'}} \tag{5.6}$$

On the other hand, from the volume occupied by the fluid in the reactor, V, and its volumetric flow rate, q, the average passage time in the reactor, τ_p, is obtained. For a circulation time much longer than the vertical flow time, $\tau_p >> \tau_{vertical}$, it can be inferred that the fluid is uniformly distributed in the vertical direction, which is also the direction of solar light incidence, i.e., all the fluid elements end up spending about the same time in the illuminated region of the RPR.

For the case under study, the above assumption is valid since $\tau_p \approx$ 144.8 s, which is much higher than the $\tau_{vertical} \approx$ 5.4 s. With these data it is expected that on average each fluid element should be on the raceway surface 13 times in each lap for the dimensions under study. Thus, it is confirmed that the implemented velocity and sludge height allow to obtain a good level of vertical mixing, so these guidelines should be followed whenever possible.

Another consideration that has to be taken into account is that the velocity component in the y direction must be superior to the particles' settling velocity, v_t . So, the velocity at which the particles start to sediment was determined in agreement with the Stoke's law [64] described in Appendix C.

According to a recent characterisation, the sludge mean particle diameter was identified as approximately 50 µm. It must be noted that this value may change depending on the characteristics of the sludge sample. Thus, considering a particles' density of 1.06 g·mL^{-1} [65], it was obtained a settling velocity of 3.4 × 10^{-4} m·s^{-1}. Therefore, as $v_t \ll \overline{v'}$, it can be inferred that the velocity in the vertical direction is sufficient to keep the particles in suspension, and, as such, to avoid sedimentation and solids accumulation in the bottom of the RPR. On the other hand, it is possible to determine the maximum radius that the particles can have to prevent sedimentation, such that $v_t = \overline{v'}$. Thus, for the situation under analysis, the particles may have a maximum size of 370 µm.

Tracer experiment validation

Furthermore, a tracer injection was performed to demonstrate that the result obtained by the previously described methodology is sufficiently conservative, i.e., it presents some margin of confidence. As such, the diffusion of the tracer plume was considered as a measure of the degree of vertical mixing.

In the tracer experiment, a velocity of 0.3 m·s^{-1} and atmospheric pressure were imposed respectively at the inlet and outlet. Then, the tracer was fed at a point in the middle of the inlet section. Figure 18 shows the mass fraction contour lines of tracer. Hence, the isoline corresponding to the outermost contour plots of the stream was chosen and its inclination was computed.

From the slope of the mentioned line, i_s, and the velocity of the fluid in the direction of the flow, u, the fluid velocity in the vertical direction, $\overline{v'}$, can be calculated by

$$\overline{v'} = i_s \, u \qquad (5.7)$$

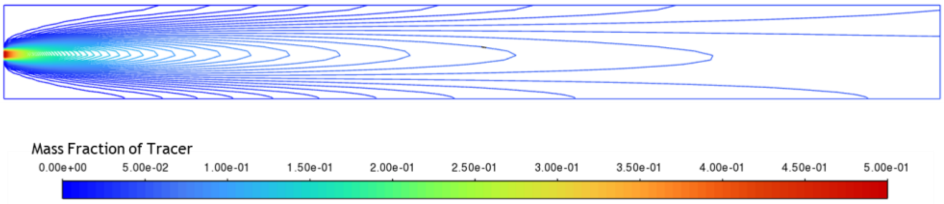

Figure 18.Contour plots of mass fraction of tracer.

It was obtained an i_s of 170.5 mm·s^{-1} and a $\overline{v'}$ of 5.11×10^{-2} m·s^{-1}. Now, in a similar way as described above, the value of $\tau_{vertical}$ was determined and compared with the value of τ_p. In this case, the difference proved to be even greater, obtaining a $\tau_{vertical}$ of 2.0 s. So, it is possible to conclude that the result previously obtained can be considered valid, proving to be sufficiently conservative and reliable.

Probability Density Function Analysis

A probability density function (PDF) of the particles' ID and y position data exported from the k-ε simulation with DPM was determined. The concept of PDF is explained in more detail in Appendix D. To perform that analysis, the Discrete Phase Model with discrete random walk was used. Accordingly, the trajectories of 29 particles were monitored. In this sense, it was possible to determine the probability of a particle to be in each y position range of the RPR depth at any time. This probability is given by the area under the PDF curve between the two desired positions. The PDF plot is shown in Figure 19. It should be noted that the point $y/y^* = 0$ is equivalent to the top of the RPR, while the point $y/y^* = 1$ corresponds to the bottom.

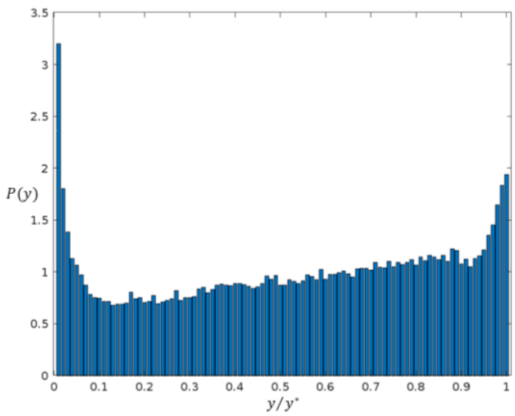

Figure 19. PDF of particles' y position.

Figure 19 shows a good distribution of the particles in the vertical direction of the RPR. Although, as expected, there is a greater probability of the particles' moving towards the top and bottom of the RPR. In between the top surface and bottom wall of the reactor, there is a higher kinetic energy that is related to the larger mixing degree due to the vortices formed, which causes the particles to acquire higher velocities and spend less time on the same position. Moreover, due to the boundary conditions of no slip at the bottom and shear stresses of zero at the top of the RPR, the particles have more difficulty to move and tend to remain there for longer periods. Therefore, the results deviate from the initial premise that mixing in the vertical direction achieves a perfect degree. Nonetheless, there is a good degree of uniformity, so the conclusions earlier drawn are not too far from reality.

5.2.4 Turbulent shear stresses

Turbulent shear stresses play a crucial role in comprehending sludge disintegration. In turbulent flows, the total shear stress corresponds to the sum of viscous and turbulent shear stresses. The exchange of momentum by turbulent stresses occurs at a larger scale than the molecular motions involved in the viscous stresses and, consequently, is much more efficient. Hence, the contribution of the viscous stresses to the total shear stress can be considered negligible [66].

The shear stresses are associated to the fluctuating strain rate, s_{ij}', that is related with the energy dissipation rate, ε, and with the kinematic viscosity of the fluid, ν, by

$$\varepsilon = 2\,\nu\,\overline{s_{ij}'s_{ji}'} = 2\,\nu\,\overline{\frac{\partial u_i'}{\partial x_j}\frac{\partial u_j'}{\partial x_i}} \quad (5.8)$$

Accordingly, the turbulent shear stress, τ_{ij}, can be determined in agreement with the Boussinesq hypothesis, reported in Section 3.1.1, from which it can be inferred that the turbulent stresses tend to increase as the mean rate of deformation increases.

Thus, for this case it was obtained a rate of deformation of 22 s^{-1} and a τ_{ij} of 0.36 Pa. This stress should be compared with the cell tensile strength, τ_s, in such a way that if $\tau_{ij} > \tau_s$, the rupture of the cells and consequent release of the content in its interior will occur, making it more bioavailable for the microorganisms present in AD.

5.2.5 Radiation Analysis

Since solar radiation has a significant impact in sludge disintegration, the importance of its study in this work becomes evident. Thus, the radiation profile along the sludge depth was determined.

For this purpose, some concepts need to be understood. Firstly, it is necessary to know the absorbance of the sludge under study in the range of ultraviolet A (UVA) radiation, between 315 and 400 nm, which is the main radiation responsible for the sludge hydrolysis effect. In this sense, an analysis was performed in a UV-Vis spectrophotometer Spectroquant® Prove 300, in which the absorbance spectrum of the sample was obtained and can be found in Appendix E.

With the values determined, an average absorbance of 89.1 was obtained for the sludge sample under study. Thus, the intensity of the radiation passing through the sludge in the direction of solar light penetration, I, was measured, considering Lambert Beer's law [67] as follows,

$$I = I_0 \times 10^{-\frac{A_b}{l_b}\times h} \quad (5.9)$$

in which A_b is the absorbance of the sample, I_0 is the intensity of the incident UVA radiation, l_b is the width of the cuvette, in this case 1 cm, and h is the sludge depth at which I is being determined.

The value of I_0 depends on several aspects, including the latitude, the longitude, the time of the year and the time of the day, so it is something to be taken into account when studying an RPR. In Portugal, near Porto, the average value of I_0 along the year is 20 W·m^{-2} [68], which was assumed for the calculations. Figure 20 shows the radiation profile along the vertical direction of the sludge.

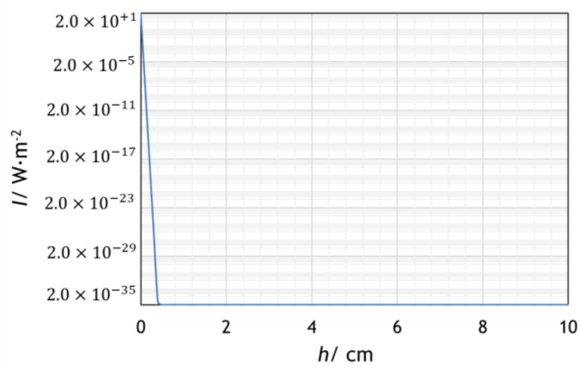

Figure 20. Radiation profile over the sludge depth.

Figure 20 shows that the penetration height of UVA radiation into the sludge is less than 1 mm. This emphasises the importance of obtaining a good degree of mixing in the direction of solar light incidence. This guarantees that all the elements present in the sludge receive the same intensity of radiation throughout the day.

Along with the intensity of radiation, the total energy received by WAS during a treatment cycle, E_t, may also be determined. For that purpose, the data obtained from the PDF becomes useful as it enables to know the percentage of time that each particle is expected to pass in a given section of the RPR depth. Hence, E_t can be calculated from the probability of each fluid element at y, having a radiation intensity $I(y)$, as follows,

$$E_t = \int_0^{t_c} \int_0^{h} P(y)\, I(y)\; dy\, dt \tag{5.10}$$

where t_c corresponds to the duration of a treatment cycle, which for the desired application is expected to be about 4 h.

Thus, each particle absorbs approximately 9208 J·m^{-2} during a treatment cycle of 4 hours. Furthermore, since WAS has an experimental average solids content of 18 g·kg^{-1}, the energy absorbed per kg of total solids was determined to compare to the data available in the literature. The value obtained, 512 kJ·(kg TS)$^{-1}$, is within the ranges of energy values that showed a good efficiency in the pre-treatments already studied in the literature, reported in Section 2.2 of this work. Therefore, the UVA radiation received by WAS is enough to promote sludge disintegration and its consequent hydrolysis in AD. In addition, it should be taken into account that t_c can be adapted according to the characteristics of the sludge and the intensity of the incident radiation, I. Thus, obtaining a higher or lower energy input is possible depending on the desired treatment level and the process conditions. Additionally, there is the advantage of the energy source being endless, which may substantially reduce the energy consumption in the process.

6 Flow Circulation

6.1 CFD Model

The last part of the work evaluates the fluid circulation system of RPRs. Thus, the rotary machine (paddlewheel) operational behaviour was analysed, considering the multiphase flow and, as such, the air-water interaction. Moreover, the efficiency of the paddlewheel was compared with other fluid propulsion systems.

6.1.1 Geometry

The geometry of the designed paddlewheel and the respective dimensions are presented in Figure 21. It should be noted that two geometries with different paddlewheel diameters were tested in order to compare the efficiency of both. The respective dimensions are given in Table 5. The paddlewheel consists of 6 paddles equally distanced. At 10 cm from the bottom there is an interface between the fluid, water, and the atmosphere. The paddle radius used in Padd2 is twice the paddle radius defined in Padd1. For Padd1, this interface coincides with the rotation center of the paddlewheel, while for Padd2 the rotational axis is above the air-water interface, so the air domain is larger. Moreover, for Padd1 only two paddles are submerged into the medium at the same time, while for Padd2 three paddles are under the interface simultaneously.

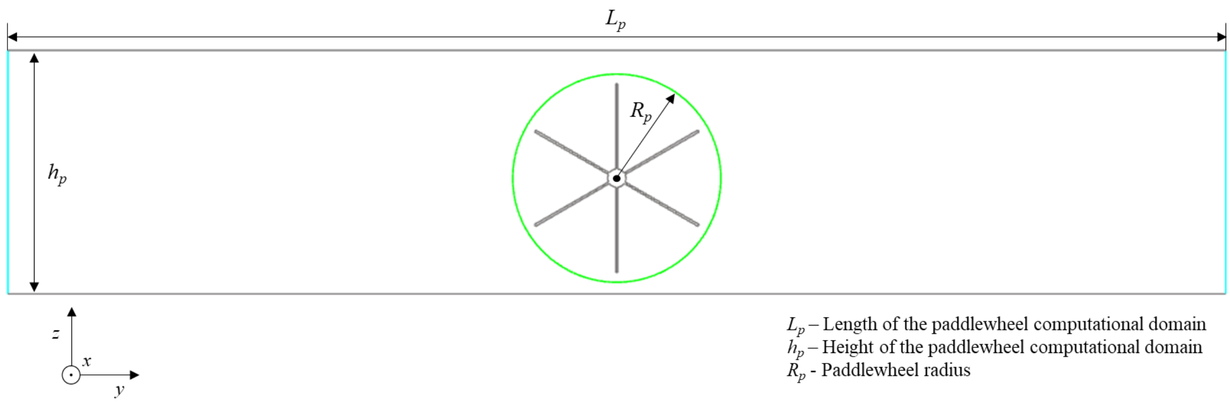

Figure 21. Rotary machine 2D geometry.

Table 5. Dimensions of the paddlewheel computational domain for the two cases studied.

	R_p/cm	h_p/cm
Padd1	17.09	20
Padd2	34.18	40

6.1.2 Boundary Conditions

In this part of the work, translational PBCs were implemented on the left and right-hand sides, which are represented by the blue lines in Figure 21. For this case, the value of $\Delta p/L$ was defined as zero, in order to only account for the energy injected into the flow by the paddlewheel. Some tests were performed with $\Delta p/L \neq 0$, that resulted in a change in the interface position with the water level gradually tending to zero, which is not as intended.

Regarding the bottom wall, a no-slip condition was imposed. In addition, at the top shear stresses of zero were established to consider the interface with the surrounding atmosphere.

The green line in Figure 21 attests for the interface between the mesh's rotational and stationary zones, i.e., between the inner and outer zones of the line, respectively. The methodology used to set up these two zones is explained in Section 6.1.4.

6.1.3 Solution methods

The methods used are described in Section 4.1.3, except for the spatial discretization of the pressure, in which the PRESTO! method was chosen. The simulations were carried out in transient state to account for the mesh motion of the domain. Thus, the methodology explained in Section 5.1.3 was followed to perform the unsteady simulations. For this case, the second order implicit method was defined for the transient formulation. The multiphase VOF model was used, and the spatial discretization of the volume fraction was set as compressive.

6.1.4 Mesh

For the flow circulation analysis, the geometry was discretized using a grid with an element size of 0.005 m for the stationary zone and an element size of 0.001 m for the rotational zone. The mesh was generated using the quadrilateral dominant method and a body sizing was inserted in the rotational zone of the grid. At the bottom wall and at the paddle walls inflation with 10 maximum layers and 1.2 growth rate was used.

To set up the mesh motion in the computational domain, it was necessary to create a non-conformal boundary between the inner and outer regions of the green interface depicted in Figure 21. The transition of both meshes was made from the sliding mesh model implemented in ANSYS Fluent. As long as the interfaces remain in contact with each other, the non-conformal interfaces are dynamically updated while the meshes are in motion, allowing the fluid to flow between the different regions. The sliding mesh model is explained in more detail in Appendix F.

Figure 22 provides a comprehensive depiction of the mesh characteristics. Furthermore, it includes a magnified view specifically focused on the rotational region, showing the inflation present in the paddle walls.

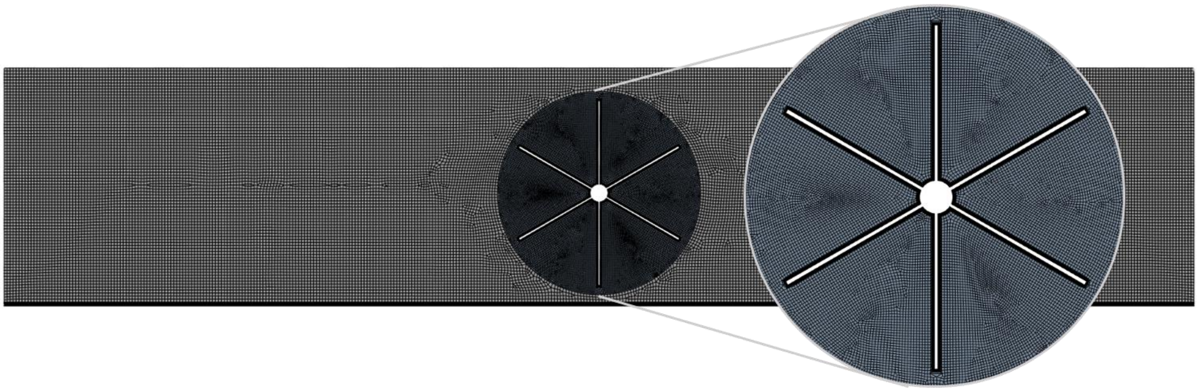

Figure 22. Mesh details of the paddlewheel geometry domain.

6.2 Results

6.2.1 Power Consumption

Several values of L_p were evaluated, i.e., the length of the domain was changed, to assess the stability of the flow and try to find a result independent of it. The mass flowrate of water on the left and right-hand sides and the torque exerted on the blades were the parameters used to evaluate this dependence.

For the aforementioned study, Padd2 geometry was used, and values of 2, 4, 8 and 16 m were assigned to L_p. The blades tip rotation speed was set to 0.3 m·s^{-1}, corresponding to approximately 17 rpm,

$$u = R_p\, \omega = \frac{2\pi\, R_p\, N}{60} \tag{6.1}$$

where R_p is the paddle radius, ω is the angular velocity in rad·s^{-1} and N corresponds to the paddle's velocity in rotations per minute, rpm.

Figure 23 shows the mass flowrate of water and the moment of the force exerted on the paddle walls as a function of the time for the different geometries analysed. The results presented were obtained after a time step where the flow oscillation kept the same pattern: quasi-steady state.

According to Figure 23, there is a certain periodicity in the flow promoted by the passage of the blades. Thus, waves are generated along the domain, reflecting the propellation effect of each paddle.

Nonetheless, it has been observed that the flow exhibits significant instability, characterized by fluctuations in Figure 23. As the domain length increases, substantial flowrate variations are observed, indicating the flow's inherent instability. Consequently, the value of $\dot{m}$ exhibits a notable variation with L_p. This variation gradually diminishes with the channel length, with the case $L_p = 16$ m getting quite close to the $L_p = 8$ m case. The flow variation is associated to the liquid lamina rippling caused by the paddles passage. Longer channels keep the boundary conditions on the blades' left and right-hand sides further apart, promoting a more constant flow.

ANSYS Fluent computes the torque or moment over the paddlewheels, T_r, as explained in Appendix G. Analysing Figure 23 in terms of the torque applied to the paddles, there is a considerable fluctuation in the values. However, there is a consistent oscillation trend, and the range of values remains similar across different cases.

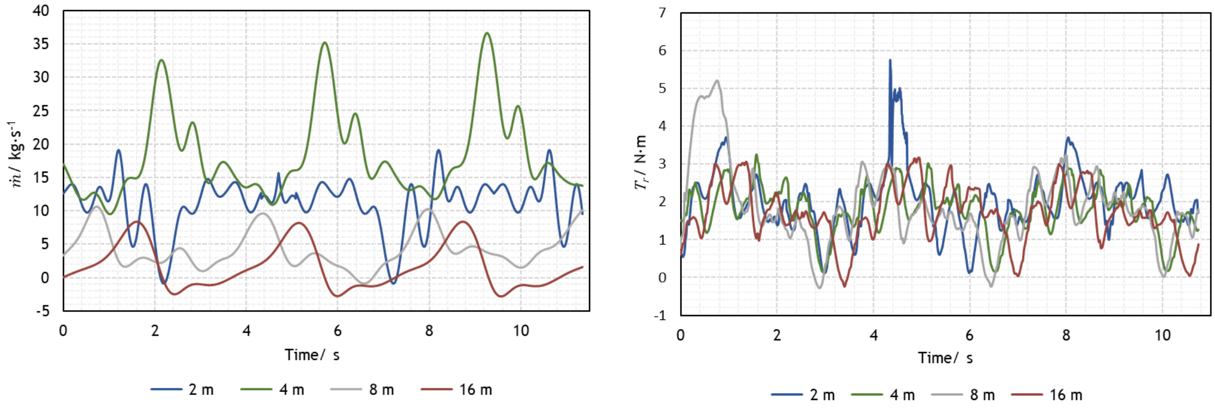

Figure 23. Mass flowrate of water, left, and moment of the force exerted on the paddle walls, right, for the different values of L_p simulated.

In this sense, the case $L_p = 16\ \mathrm{m}$ was chosen to proceed with the calculations of the paddlewheel efficiency because it is less affected by the paddles rippling effect over the water lamina, and the sensitivity analysis shows that for $L_p > 8\ \mathrm{m}$ the flow features are only slightly affected. To this end, the angular velocity of the impeller was incremented, as the velocity imposed on the flow was too low for the intended application. As so, it was considered that $\omega = 20$ rad·s^{-1} for Padd2 geometry and $\omega = 40$ rad·s^{-1} for Padd1 geometry since $R_{Padd2}/R_{Padd1} = 2$.

The power supplied by the paddlewheel, P_s, is the scalar product of torque, T_r, and angular velocity [69] as follows,

$$P_s = T_r\ \omega \tag{6.2}$$

On the other hand, the power of the flow, P_f, was calculated considering the geometry provided in Section 5.1.1. This is the power expended by the flow to maintain the same velocity imposed by the paddlewheel. So, considering the power as the product of the flow rate by the pressure difference along the 16 m of the domain, it can be calculated by,

$$P_f = \Delta p\ q \tag{6.3}$$

Therefore, the efficiency of the paddlewheel, η, is given by,

$$\eta\ (\%) = 100 \frac{P_f}{P_s} \tag{6.4}$$

Table 6 summarizes the results obtained for the 2 geometries studied.

Table 6. Results and efficiency of each paddlewheel studied.

	q/ m^3·s^{-1}	T_r/ N·m	Δp/ Pa	P_s/ W	P_f/ W	η/ %
Padd1	0.003	1.2	0.6	48.7	0.002	0.004
Padd2	0.02	6.7	14.7	133.5	0.3	0.2

From the analysis of the results, it is clear that the use of a paddlewheel to promote the sludge flow is very inefficient, especially for such low liquid depths. This agrees with the results reported in the literature, which indicate efficiencies of less than 7 % [70]. This value was obtained by considering a typical slope determined by Manning's equation for the reported velocity and comparing it with the supplied power in W·m^{-2}, assuming a basis of calculation of 1 m. It should be noted that the liquid depth was 30 cm, which justifies the higher efficiency compared to that obtained in this work.

In addition, it can be reported that Padd2 is more efficient in transmitting energy to the fluid by dissipating less mechanical power, so increasing the diameter of the paddles is advantageous and results in a better efficiency. It is important to note that in both cases it was not possible to reach a velocity of 0.3 m·s^{-1} in the flow, so the rotation speed of the paddles should be even higher.

The contour plots of volume fraction of water for Padd2 geometry are shown in Figure 24. It shows the evolution of the interface air-water with time. The upper case corresponds to the initial state, while the other pictures represent subsequent time steps.

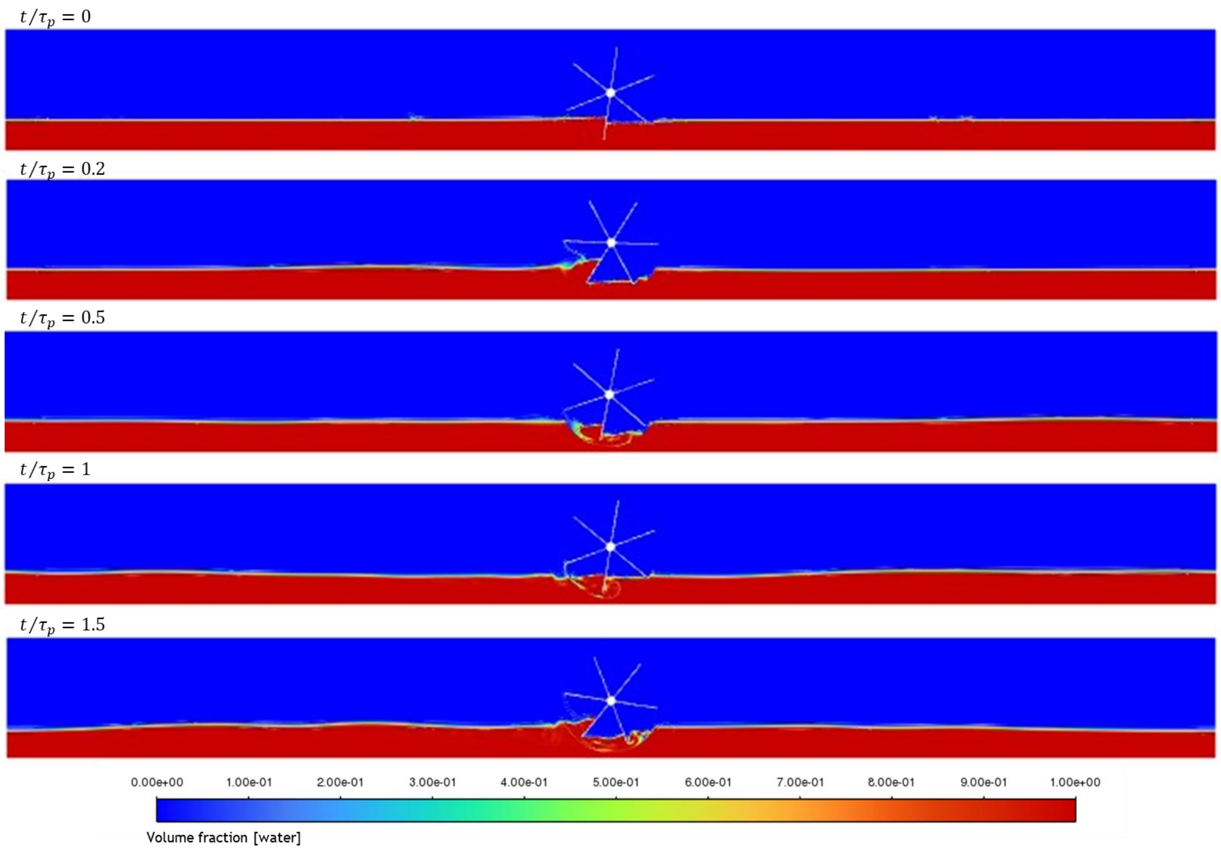

Figure 24. Volume fraction of water for Padd2 geometry over time.

Figure 24 shows that the largest mass transfer is equivalent to the zone where the paddlewheel agitation occurs, as expected. Furthermore, the waves propelled by the paddlewheel movement can be observed along the entire domain interface, which confirms the flow oscillation previously verified by the graphical representation in Figure 23.

It is important to consider that this work only consists of an initial effort to optimise the shape of the paddles for improved paddlewheel efficiency. The model should also undergo a more extensive verification regarding turbulence models, wall functions, and solver methods. After verification, since the flow turbulence is modelled at the sub-grid scale the flow should also be validated from experimental data. Additionally, a comprehensive optimisation study must be carried out to attain an optimal blade paddle shape that maximizes the effectiveness of this system. This study should include defining the blade number, blade length, and blade curvature as design variables, and assessing their impact on the overall performance of the existing circulation system.

The application of RPRs for WAS pre-treatment makes it necessary to impose low liquid heights due to the high absorbance of the sludge, which is one of the main reasons for the low efficiency of these impellers. In this way, the study of some fluid circulation alternatives seems to be interesting.

6.2.2 Paddlewheel vs Pump Recirculation

A promising alternative to the fluid circulation imposed by a paddlewheel is a configuration with a recirculation pump and a distributor. Figure 25 shows a schematic representation of the perspective view of this geometry. In this representation, the fluid flows due to the inclination of the reactor channels. A distributor at the top ramps of the raceway distributes the flow by the two ramps on each side. These ramps extend to the end of the raceway where the direction of flow is inverted. After the flow is reversed, a ramp ends on each side of the RPR towards the collector, which consists of a tank inserted in the bottom of the reactor. This tank feeds the recirculation pump, which supplies the fluid to the distributor on the opposite side of the raceway.

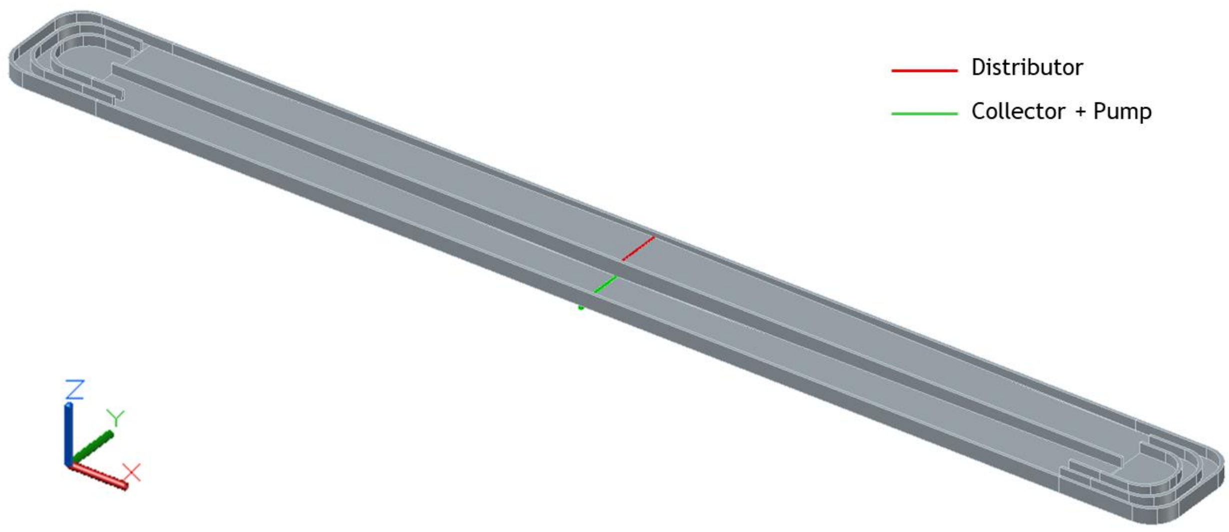

Figure 25. Sloped geometry perspective view.

In order to compare the two situations under analysis, the pump sizing was studied.

The pump net power, i.e., the energy transferred on the fluid being pumped to increase its pressure and velocity, is given by Equation 6.3, wherein the flowrate corresponds to the product of the velocity by the area of the straight section and the pressure gain is given by,

$$\Delta p = \rho\, g\, H \tag{6.5}$$

where H is the manometric head of the pump and by definition is equivalent to the energy per unit weight of the fluid in circulation. The value of H is a characteristic of the pump and is equal to the losses at the pump and along the pipeline connecting the collector to the distributor [64]. Thus H is given by

$$H = \Delta z + h_m + h_f \tag{6.6}$$

where Δz represents the elevation difference between the two sides of the RPR, i.e., the lifting height of the fluid, h_m correspond to minor losses, i.e., additional losses due to the entry, elbow and exit of the pipe, and h_f is the pipeline friction losses.

Hence, Δz can be calculated by,

$$\Delta z = L_r\, S + l \tag{6.7}$$

where the value of S is determined by the Manning's equation, described above in Section 5.1.2, L_r is the length of the reactor and l is an additional height considered for the collector tank, which was assumed to be 0.5 m.

The minor losses, h_m are given by

$$h_m = \sum K \frac{v_p^2}{2g} \tag{6.8}$$

in which v_p is the velocity in the pipe, and K is the loss coefficient that can be considered 1.5 for the elbow and 0.5 for the pipeline entrance and exit.

The friction losses, h_f, can be described by Hazen-Williams equation as follows

$$h_f = \frac{10.67\, L_f\, q^{1.85}}{C^{1.85}\, d^{4.87}} \tag{6.9}$$

where L_f is the length of pipe, assumed as 4 m, C is a roughness coefficient, 140 for smooth pipes, and d represents inside pipe diameter, considering a standard size of 4 inch, equivalent to 0.1 m.

Assuming the dimensions described in Section 4.1.1, L_r corresponds to 22 m. Thus, the aforementioned geometry presents a total head loss, H, of 2.9 m. With these data, the mechanical power received by the fluid is about 846 W. So, for these specifications, the pump will have an efficiency of about 47 % according to the dimensioning data from the supplier Grundfos.

Hence, despite the enhanced efficiency of this configuration, the energy demand for fluid pumping, approximately 1800 W, significantly exceeds the energy utilized by the paddlewheel for fluid agitation. For the paddlewheel case, assuming a behaviour similar to the cases previously studied, it is possible to estimate the power to be supplied to maintain the same flow velocity of 0.3 $m \cdot s^{-1}$. Thus, making an extrapolation of the values and assuming an efficiency for the electric motor of 80 %, a power of 250 W was estimated. As a result, although an increase in paddle rotation speed is required to achieve the desired flow velocity, it is unlikely to reach power levels as high as those observed in the sloped geometry, considering the previous results. Therefore, the paddlewheel propeller might be a better option as far as energy requirements are concerned. Nevertheless, the optimisation of the hydraulic circuit in the inclined geometry should be a factor to take into account in order to reduce its energy consumption and make this configuration a more competitive alternative.

7 Conclusion

Currently, the establishment of WAS pre-treatments that are both highly efficient and cost-effective remains a significant challenge. The significance of this issue extends beyond merely disintegrating sludge structure. It represents a strategic approach aimed at producing solid sludge of adequate quality for soil enrichment while preventing contamination. Furthermore, this approach plays a crucial role in advancing renewable energy sources, potentially revolutionizing the energy landscape of WWTPs and the world at large.

The application of RPRs for this purpose is very promising due to its many advantages, namely low cost in comparison with other methods. In this work, the design of these reactors was studied using CFD tools and some theoretical correlations. Additionally, design guidelines are presented to provide information regarding optimisation of the various reactor design components.

Regarding the overall flow design, there are some aspects to consider when designing a RPR. The best geometry comprises the implementation of flow deflectors on the RPR U-turn. It enables a decrease in pressure drop and energy dissipation in the U-shaped curve of the RPR. The longer flow deflectors at the outlet of the RPR bend help to uniformize the flow and minimize vortex at this position. The length to width ratio should be considered to scale up this reactor. Ideally a ratio of L_r/w_r of 10, as presented here, is considered adequate. Increasing the number of baffles in proportion to the reactor dimensions is also something to consider when scaling up the reactor.

Concerning the vertical flow, the RPR under study has proven to have a good performance in mixing the fluid vertically. Accordingly, the velocity fluctuations in the y direction have shown to be sufficient to promote the mixing of the sludge, avoiding property gradients in the light incidence direction. Similarly, the PDF of the particles' y position indicates a good distribution. Nevertheless, the most energetic eddies in the middle section of the reactor depth force the particles to move to the extremes, remaining there longer periods comparatively with the rest of the domain. With regard to the radiation analysis, RPR seems very advantageous for solar applications like WAS pre-treatment as it enables the energy input to be easily adjusted by changing the process conditions. Furthermore, an additional benefit lies in the potential for attaining high energy inputs through an endless energy source, which promises to significantly reduce energy consumption in the process.

Regarding the flow circulation, the study of the paddlewheel impeller has become challenging due to the flow instability and limitations of the numerical simulations. Nonetheless, this impeller design has demonstrated notably low efficiencies, suggesting it may not be suitable for applications involving such small fluid depths. On the other hand, the implementation of a sloped geometry appears to offer a worst option regarding the energy requirements. In this sense, better solutions for the fluid circulation must be studied. However, further studies concerning CFD numerical model verification and experimental validation of the presented configurations are needed to take proper conclusions.

The diagram in Figure 26 aims to summarise the key aspects of this work and the guidelines to follow with regard to the design of RPRs.

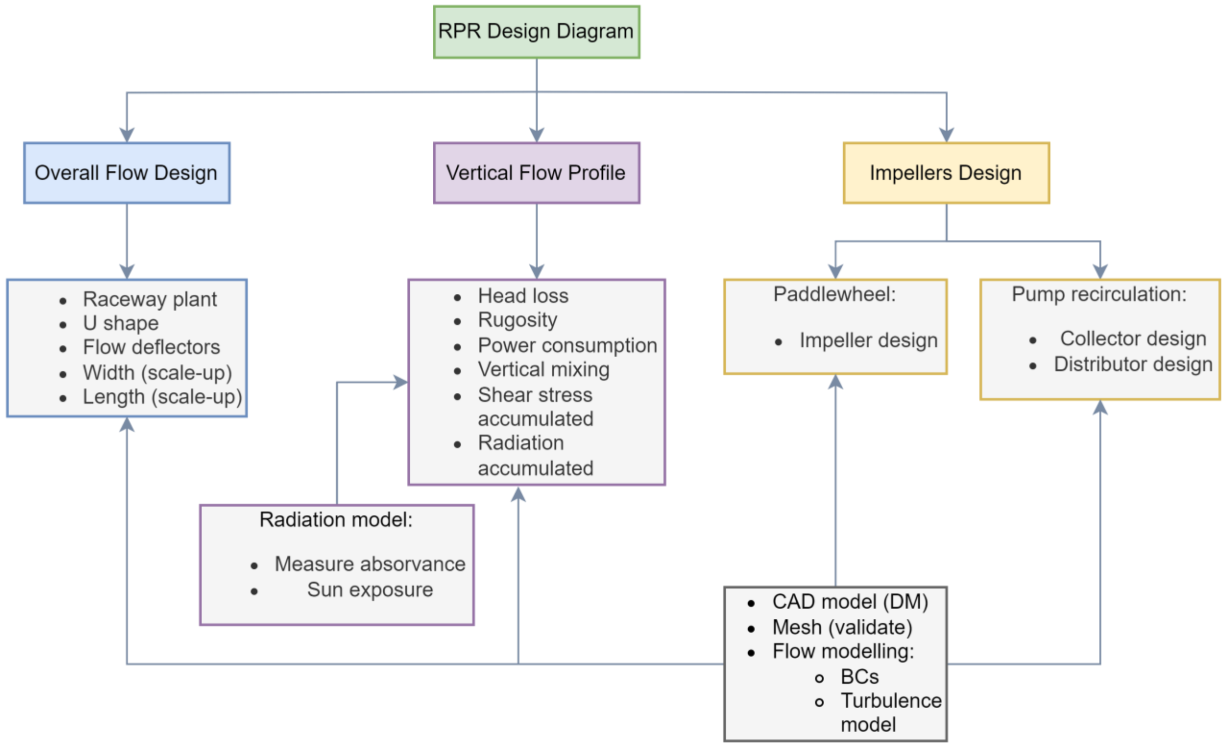

Figure 26. RPR Design Diagram.

8 Assessment of the work done

8.1 Objectives Achieved and Future Work

The main objective of this work was to study the design of a RPR applied to the pre-treatment of WAS using CFD tools. It was accomplished by characterizing the overall flow design, the vertical flow, and the flow circulation system. The suitability of these devices was substantiated by their successful implementation of flow deflectors, effective attainment of a significant level of vertical mixing, and demonstrated effectiveness for applications reliant on radiation. Moreover, investigations have revealed that a paddlewheel propeller offers improved energy consumption for fluid circulation than an inclined geometry, coupled with a pump and a distributor. However, further studies are needed to investigate this topic in greater detail.

As future work some suggestions are presented below:

- Conduct a verification of the numerical results by comparing it with those obtained from a fluid with similar characteristics to WAS, as it is expected to have higher viscosity than water.
- Check other turbulence models like Large Eddy Simulation, calculating even the small vortices.
- Validate the 2D approach proposed in this work by performing 3D simulations.
- Validate experimentally the results regarding: the measurement of chemical aspects that affect WAS disintegration; placement of a heat insulation material (transmissive to solar light) over the RPR resulting in a greenhouse effect to enable WAS temperatures of 60-80 °C; placement of curved baffles at the bottom of the RPR to improve vertical and horizontal fluid mixing, enhancing the flashing light effect.

8.2 Final Assessment

During the dissertation's work the major limitation was the time expended for the verification of the numerical results, regarding models, near-wall treatment and meshes validation. The design of the geometries in Design Modeler was also a very time-consuming process, which did not allow much time for the improvement of the results as well as testing different models and approaches to simulate the RPR.

Additionally, the transient simulations performed in the study of the flow circulation were very unstable, which required very large simulation times to obtain minimally reliable results.

9 References

1. Shen, Y., J.L. Linville, M. Urgun-Demirtas, M.M. Mintz, and S.W. Snyder, *An overview of biogas production and utilization at full-scale wastewater treatment plants (WWTPs) in the United States: Challenges and opportunities towards energy-neutral WWTPs*. Renewable and Sustainable Energy Reviews, 2015. **50**: p. 346-362 DOI: 10.1016/j.rser.2015.04.129.

2. Wacławek, S., K. Grübel, D. Silvestri, V.V.T. Padil, M. Wacławek, M. Černík, and R.S. Varma, *Disintegration of Wastewater Activated Sludge (WAS) for Improved Biogas Production*. Energies, 2019. **12**(1): p. 21 DOI: 10.3390/en12010021.

3. Halleux, V., *Urban wastewater treatment: Updating EU rules*. 2023.

4. Gonzalez, A., A.T.W.M. Hendriks, J.B. van Lier, and M. de Kreuk, *Pre-treatments to enhance the biodegradability of waste activated sludge: Elucidating the rate limiting step*. Biotechnology Advances, 2018. **36**(5): p. 1434-1469 DOI: 10.1016/j.biotechadv.2018.06.001.

5. Hreiz, R., B. Sialve, J. Morchain, R. Escudié, J.-P. Steyer, and P. Guiraud, *Experimental and numerical investigation of hydrodynamics in raceway reactors used for algaculture*. Chemical Engineering Journal, 2014. **250**: p. 230-239 DOI: 10.1016/j.cej.2014.03.027.

6. Peralta Muniz Moreira, R., A. Cabrera Reina, P. Soriano Molina, J.A. Sánchez Pérez, and G. Li Puma, *Computational fluid dynamics (CFD) modeling of removal of contaminants of emerging concern in solar photo-Fenton raceway pond reactors*. Chemical Engineering Journal, 2021. **413**: p. 127392 DOI: 10.1016/j.cej.2020.127392.

7. Hreiz, R., M.A. Latifi, and N. Roche, *Optimal design and operation of activated sludge processes: State-of-the-art*. Chemical Engineering Journal, 2015. **281**: p. 900-920 DOI: 10.1016/j.cej.2015.06.125.

8. Syed R. Qasim, G.Z., *Wastewater Treatment and Reuse Theory and Design Examples, Volume1: Principles and Basic Treatment (1st ed)*. 1st ed. Vol. 1. 2017: CRC Press.

9. Khanh Nguyen, V., D. Kumar Chaudhary, R. Hari Dahal, N. Hoang Trinh, J. Kim, S.W. Chang, Y. Hong, D. Duc La, X.C. Nguyen, H. Hao Ngo, W.J. Chung, and D.D. Nguyen, *Review on pretreatment techniques to improve anaerobic digestion of sewage sludge*. Fuel, 2021. **285**: p. 119105 DOI: 10.1016/j.fuel.2020.119105.

10. Azarmanesh, R., M. Zarghami Qaretapeh, M. Hasani Zonoozi, H. Ghiasinejad, and Y. Zhang, *Anaerobic co-digestion of sewage sludge with other organic wastes: A comprehensive review focusing on selection criteria, operational conditions, and microbiology*. Chemical Engineering Journal Advances, 2023. **14**: p. 100453 DOI: 10.1016/j.ceja.2023.100453.

11. Appels, L., J. Baeyens, J. Degrève, and R. Dewil, *Principles and potential of the anaerobic digestion of waste-activated sludge*. Progress in Energy and Combustion Science, 2008. **34**(6): p. 755-781 DOI: 10.1016/j.pecs.2008.06.002.

12. Huang, F., H. Liu, J. Wen, C. Zhao, L. Dong, and H. Liu, *Underestimated humic acids release and influence on anaerobic digestion during sludge thermal hydrolysis*. Water Research, 2021. **201**: p. 117310 DOI: 10.1016/j.watres.2021.117310.

13. Tena, M., M. Perez, and R. Solera, *Effects of several inocula on the biochemical hydrogen potential of sludge-vinasse co-digestion*. Fuel, 2019. **258**: p. 116180 DOI: 10.1016/j.fuel.2019.116180.

14. Sembera, C., C. Macintosh, S. Astals, and K. Koch, *Benefits and drawbacks of food and dairy waste co-digestion at a high organic loading rate: A Moosburg WWTP case study*. Waste Management, 2019. **95**: p. 217-226 DOI: 10.1016/j.wasman.2019.06.008.

15. Bachmann, N., *Sustainable biogas production in municipal wastewater treatment plants*. 2015, IEA Bioenergy.

16. Santos, E., A. Albuquerque, I. Lisboa, P. Murray, and H. Ermis, *Economic Assessment of Energy Consumption in Wastewater Treatment Plants: Applicability of Alternative Nature-Based Technologies in Portugal*. Water, 2022. **14**(13): p. 2042 DOI: 10.3390/w14132042.

17. Guo, Z., Y. Sun, S.-Y. Pan, and P.-C. Chiang, *Integration of Green Energy and Advanced Energy-Efficient Technologies for Municipal Wastewater Treatment Plants*. International Journal of Environmental Research and Public Health, 2019. **16**: p. 1282 DOI: 10.3390/ijerph16071282.

18. Portugal, Á.d. *ETAR da Guia é 100% autossuficiente em energia*. 2017 [cited 2023 May 5]; Available from: https://www.adp.pt/pt/?id=69&idn=139.

19. Green, S.o. *Marselisborg WWTP – from wastewater plant to power plant*. 2016 [cited 2023 May 5]; Available from: https://stateofgreen.com/en/solutions/marselisborg-wwtp-energy-neutral-water-management/.

20. Shrestha, B., R. Hernandez, D.L.B. Fortela, W. Sharp, A. Chistoserdov, D. Gang, E. Revellame, W. Holmes, and M.E. Zappi, *A Review of Pretreatment Methods to Enhance Solids Reduction during Anaerobic Digestion of Municipal Wastewater Sludges and the Resulting Digester Performance: Implications to Future Urban Biorefineries*. Applied Sciences, 2020. **10**(24): p. 9141 DOI: 10.3390/app10249141.

21. Mitraka, G.-C., K.N. Kontogiannopoulos, M. Batsioula, G.F. Banias, A.I. Zouboulis, and P.G. Kougias, *A Comprehensive Review on Pretreatment Methods for Enhanced Biogas Production from Sewage Sludge*. Energies, 2022. **15**(18): p. 6536 DOI: 10.3390/en15186536.

22. Volschan Junior, I., R. de Almeida, and M.C. Cammarota, *A review of sludge pretreatment methods and co-digestion to boost biogas production and energy self-sufficiency in wastewater treatment plants*. Journal of Water Process Engineering, 2021. **40**: p. 101857 DOI: 10.1016/j.jwpe.2020.101857.

23. Li, X., S. Guo, Y. Peng, Y. He, S. Wang, L. Li, and M. Zhao, *Anaerobic digestion using ultrasound as pretreatment approach: Changes in waste activated sludge, anaerobic digestion performances and digestive microbial populations*. Biochemical Engineering Journal, 2018. **139**: p. 139-145 DOI: 10.1016/j.bej.2017.11.009.

24. Sahinkaya, S., *Disintegration of municipal waste activated sludge by simultaneous combination of acid and ultrasonic pretreatment*. Process Safety and Environmental Protection, 2015. **93**: p. 201-205 DOI: 10.1016/j.psep.2014.04.002.

25. Lizama, A.C., C.C. Figueiras, A.Z. Pedreguera, and J.E. Ruiz Espinoza, *Effect of ultrasonic pretreatment on the semicontinuous anaerobic digestion of waste activated sludge with increasing loading rates*. International Biodeterioration & Biodegradation, 2018. **130**: p. 32-39 DOI: 10.1016/j.ibiod.2018.03.013.

26. Cai, M.-Q., J.-Q. Hu, G. Wells, Y. Seo, R. Spinney, S.-H. Ho, D.D. Dionysiou, J. Su, R. Xiao, and Z. Wei, *Understanding Mechanisms of Synergy between Acidification and Ultrasound Treatments for Activated Sludge Dewatering: From Bench to Pilot-Scale Investigation*. Environmental Science & Technology, 2018. **52**(7): p. 4313-4323 DOI: 10.1021/acs.est.8b00310.

27. Appels, L., S. Houtmeyers, J. Degrève, J. Van Impe, and R. Dewil, *Influence of microwave pre-treatment on sludge solubilization and pilot scale semi-continuous anaerobic digestion*. Bioresource Technology, 2013. **128**: p. 598-603 DOI: 10.1016/j.biortech.2012.11.007.

28. Serrano, A., J.A. Siles, M.A. Martín, A.F. Chica, F.S. Estévez-Pastor, and E. Toro-Baptista, *Improvement of anaerobic digestion of sewage sludge through microwave pre-treatment*. Journal of Environmental Management, 2016. **177**: p. 231-239 DOI: 10.1016/j.jenvman.2016.03.048.

29. Mehdizadeh, S.N., C. Eskicioglu, J. Bobowski, and T. Johnson, *Conductive heating and microwave hydrolysis under identical heating profiles for advanced anaerobic digestion of municipal sludge*. Water Research, 2013. **47**(14): p. 5040-5051 DOI: 10.1016/j.watres.2013.05.055.

30. Zhang, Y., P. Zhang, B. Ma, H. Wu, S. Zhang, and X. Xu, *Sewage sludge disintegration by high-pressure homogenization: A sludge disintegration model*. Journal of Environmental Sciences, 2012. **24**(5): p. 814-820 DOI: 10.1016/S1001-0742(11)60834-6.

31. Barber, W.P.F., *Thermal hydrolysis for sewage treatment: A critical review*. Water Research, 2016. **104**: p. 53-71 DOI: 10.1016/j.watres.2016.07.069.

32. Carrère, H., C. Bougrier, D. Castets, and J.P. Delgenès, *Impact of initial biodegradability on sludge anaerobic digestion enhancement by thermal pretreatment*. Journal of Environmental Science and Health, Part A, 2008. **43**(13): p. 1551-1555 DOI: 10.1080/10934520802293735.

33. Bougrier, C., J.P. Delgenès, and H. Carrère, *Effects of thermal treatments on five different waste activated sludge samples solubilisation, physical properties and anaerobic digestion*. Chemical Engineering Journal, 2008. **139**(2): p. 236-244 DOI: 10.1016/j.cej.2007.07.099.

34. Pilli, S., S. Yan, R.D. Tyagi, and R.Y. Surampalli, *Thermal Pretreatment of Sewage Sludge to Enhance Anaerobic Digestion: A Review*. Critical Reviews in Environmental Science and Technology, 2015. **45**(6): p. 669-702 DOI: 10.1080/10643389.2013.876527.

35. Zhang, J., N. Li, X. Dai, W. Tao, I.R. Jenkinson, and Z. Li, *Enhanced dewaterability of sludge during anaerobic digestion with thermal hydrolysis pretreatment: New insights through structure evolution.* Water Research, 2018. **131**: p. 177-185 DOI: 10.1016/j.watres.2017.12.042.

36. Liao, X., H. Li, Y. Zhang, C. Liu, and Q. Chen, *Accelerated high-solids anaerobic digestion of sewage sludge using low-temperature thermal pretreatment.* International Biodeterioration & Biodegradation, 2016. **106**: p. 141-149 DOI: 10.1016/j.ibiod.2015.10.023.

37. Ruffino, B., G. Campo, G. Genon, E. Lorenzi, D. Novarino, G. Scibilia, and M. Zanetti, *Improvement of anaerobic digestion of sewage sludge in a wastewater treatment plant by means of mechanical and thermal pre-treatments: Performance, energy and economical assessment.* Bioresource Technology, 2015. **175**: p. 298-308 DOI: 10.1016/j.biortech.2014.10.071.

38. Liu, T., C. Wu, Y. Wang, G. Xue, M. Zhang, C. Liu, and Y. Zheng, *Enhanced Deep Utilization of Low-Organic Content Sludge by Processing Time-Extended Low-Temperature Thermal Pretreatment.* ACS Omega, 2021. **6**(43): p. 28946-28954 DOI: 10.1021/acsomega.1c04006.

39. Raynaud, M., J. Vaxelaire, J. Olivier, E. Dieudé-Fauvel, and J.-C. Baudez, *Compression dewatering of municipal activated sludge: Effects of salt and pH.* Water Research, 2012. **46**(14): p. 4448-4456 DOI: 10.1016/j.watres.2012.05.047.

40. Tian, X., C. Wang, A.P. Trzcinski, L. Lin, and W.J. Ng, *Insights on the solubilization products after combined alkaline and ultrasonic pre-treatment of sewage sludge.* Journal of Environmental Sciences, 2015. **29**: p. 97-105 DOI: 10.1016/j.jes.2014.07.024.

41. Shao, L., X. Wang, H. Xu, and P. He, *Enhanced anaerobic digestion and sludge dewaterability by alkaline pretreatment and its mechanism.* Journal of Environmental Sciences, 2012. **24**(10): p. 1731-1738 DOI: 10.1016/S1001-0742(11)61031-0.

42. Pilli, S., A. Pandey, A. Katiyar, K. Pandey, and R. Tyagi, *Pre-treatment Technologies to Enhance Anaerobic Digestion.* 2020.

43. Devlin, D.C., S.R.R. Esteves, R.M. Dinsdale, and A.J. Guwy, *The effect of acid pretreatment on the anaerobic digestion and dewatering of waste activated sludge.* Bioresource Technology, 2011. **102**(5): p. 4076-4082 DOI: 10.1016/j.biortech.2010.12.043.

44. Goel, R., T. Tokutomi, and H. Yasui, *Anaerobic digestion of excess activated sludge with ozone pretreatment.* Water Science and Technology, 2003. **47**(12): p. 207-214 DOI: 10.2166/wst.2003.0648.

45. Silvestre, G., B. Ruiz, M. Fiter, C. Ferrer, J.G. Berlanga, S. Alonso, and A. Canut, *Ozonation as a Pre-treatment for Anaerobic Digestion of Waste-Activated Sludge: Effect of the Ozone Doses.* Ozone: Science & Engineering, 2015. **37**(4): p. 316-322 DOI: 10.1080/01919512.2014.985817.

46. Montalvo, S., C. Huiliñir, F. Ojeda, A. Castillo, L. Lillo, and L. Guerrero, *Microaerobic pretreatment of sewage sludge: Effect of air flow rate, pretreatment time and temperature on the aerobic process and methane generation.* International Biodeterioration & Biodegradation, 2016. **110**: p. 1-7 DOI: 10.1016/j.ibiod.2016.01.010.

47. Barati Rashvanlou, R., A. Rezaee, M. Farzadkia, M. Gholami, and M. Kermani, *Effect of micro-aerobic process on improvement of anaerobic digestion sewage sludge treatment: flow cytometry and ATP assessment.* RSC Advances, 2020. **10**(59): p. 35718-35728 DOI: 10.1039/D0RA05540A.

48. Ge, H., P.D. Jensen, and D.J. Batstone, *Increased temperature in the thermophilic stage in temperature phased anaerobic digestion (TPAD) improves degradability of waste activated sludge.* Journal of Hazardous Materials, 2011. **187**(1): p. 355-361 DOI: 10.1016/j.jhazmat.2011.01.032.

49. Xin, X., J. He, L. Li, and W. Qiu, *Enzymes catalyzing pre-hydrolysis facilitated the anaerobic fermentation of waste activated sludge with acidogenic and microbiological perspectives.* Bioresource Technology, 2018. **250**: p. 69-78 DOI: 10.1016/j.biortech.2017.09.211.

50. Liew, Y.X., Y.J. Chan, S. Manickam, M.F. Chong, S. Chong, T.J. Tiong, J.W. Lim, and G.-T. Pan, *Enzymatic pretreatment to enhance anaerobic bioconversion of high strength wastewater to biogas: A review.* Science of The Total Environment, 2020. **713**: p. 136373 DOI: 10.1016/j.scitotenv.2019.136373.

51. Brémond, U., R. de Buyer, J.-P. Steyer, N. Bernet, and H. Carrere, *Biological pretreatments of biomass for improving biogas production: an overview from lab scale to full-scale.* Renewable and Sustainable Energy Reviews, 2018. **90**: p. 583-604 DOI: 10.1016/j.rser.2018.03.103.

52. Lundquist, T.J., I. Woertz, and J.R. Benemann. *Microalgae for wastewater treatment and biofuels production.* in *ABSTRACTS OF PAPERS OF THE AMERICAN CHEMICAL SOCIETY*. 2010. AMER CHEMICAL SOC 1155 16TH ST, NW, WASHINGTON, DC 20036 USA.

53. De la Obra Jiménez, I., B. Esteban García, G. Rivas Ibáñez, J.L. Casas López, and J.A. Sánchez Pérez, *Continuous flow disinfection of WWTP secondary effluents by solar photo-Fenton at neutral pH in raceway pond reactors at pilot plant scale*. Applied Catalysis B: Environmental, 2019. **247**: p. 115-123 DOI: 10.1016/j.apcatb.2019.01.093.

54. Inostroza, C., A. Solimeno, J. García, J.M. Fernández-Sevilla, and F.G. Acién, *Improvement of real-scale raceway bioreactors for microalgae production using Computational Fluid Dynamics (CFD)*. Algal Research, 2021. **54**: p. 102207 DOI: 10.1016/j.algal.2021.102207.

55. Hadiyanto, H., S. Elmore, T. Van Gerven, and A. Stankiewicz, *Hydrodynamic evaluations in high rate algae pond (HRAP) design*. Chemical Engineering Journal, 2013. **217**: p. 231-239 DOI: 10.1016/j.cej.2012.12.015.

56. Chisti, Y., *Large-Scale Production of Algal Biomass: Raceway Ponds*, in *Algae Biotechnology: Products and Processes*, F. Bux and Y. Chisti, Editors. 2016, Springer International Publishing: Cham. p. 21-40.

57. Liffman, K., D.A. Paterson, P. Liovic, and P. Bandopadhayay, *Comparing the energy efficiency of different high rate algal raceway pond designs using computational fluid dynamics*. Chemical Engineering Research and Design, 2013. **91**(2): p. 221-226 DOI: 10.1016/j.cherd.2012.08.007.

58. Sompech, K., Y. Chisti, and T. Srinophakun, *Design of raceway ponds for producing microalgae*. Biofuels, 2012. **3**(4): p. 387-397 DOI: 10.4155/bfs.12.39.

59. Huang, J., X. Qu, M. Wan, J. Ying, Y. Li, F. Zhu, J. Wang, G. Shen, J. Chen, and W. Li, *Investigation on the performance of raceway ponds with internal structures by the means of CFD simulations and experiments*. Algal Research, 2015. **10**: p. 64-71 DOI: 10.1016/j.algal.2015.04.012.

60. ANSYS, *ANSYS Fluent Theory Guide*. 2022, ANSYS, Inc: U.S.A.

61. Wang, G., F. Yang, K. Wu, Y. Ma, C. Peng, T. Liu, and L.-P. Wang, *Estimation of the dissipation rate of turbulent kinetic energy: A review*. Chemical Engineering Science, 2021. **229**: p. 116133 DOI: 10.1016/j.ces.2020.116133.

62. Sawant, S.S., S.N. Gosavi, H.P. Khadamkar, C.S. Mathpati, R. Pandit, and A.M. Lali, *Energy efficient design of high depth raceway pond using computational fluid dynamics*. Renewable Energy, 2019. **133**: p. 528-537 DOI: 10.1016/j.renene.2018.10.016.

63. Bonetti, S., G. Manoli, C. Manes, A. Porporato, and G.G. Katul, *Manning's formula and Strickler's scaling explained by a co-spectral budget model*. Journal of Fluid Mechanics, 2017. **812**: p. 1189-1212 DOI: 10.1017/jfm.2016.863.

64. Campos, J.M.d., *Mecânica dos Fluidos em Operações Unitárias*. 1st ed. 2017.

65. Dammel, E.E. and E.D. Schroeder, *Density of activated sludge solids*. Water Research, 1991. **25**(7): p. 841-846 DOI: 10.1016/0043-1354(91)90165-M.

66. H. Versteeg, W.M., *An Introduction to Computational Fluid Dynamics: The Finite Volume Method*. 2nd ed. 2007: Pearson.

67. Mayerhöfer, T.G., S. Pahlow, and J. Popp, *The Bouguer-Beer-Lambert Law: Shining Light on the Obscure*. Chemphyschem, 2020. **21**(18): p. 2029-2046 DOI: 10.1002/cphc.202000464.

68. Silva, T.F.C.V., A. Fonseca, I. Saraiva, R.A.R. Boaventura, and V.J.P. Vilar, *Scale-up and cost analysis of a photo-Fenton system for sanitary landfill leachate treatment*. Chemical Engineering Journal, 2016. **283**: p. 76-88 DOI: 10.1016/j.cej.2015.07.063.

69. Reyes, V., J.J. Rodríguez, O. Carranza, and R. Ortega. *Review of mathematical models of both the power coefficient and the torque coefficient in wind turbines*. in *2015 IEEE 24th International Symposium on Industrial Electronics (ISIE)*. 2015.

70. Rogers, J.N., J.N. Rosenberg, B.J. Guzman, V.H. Oh, L.E. Mimbela, A. Ghassemi, M.J. Betenbaugh, G.A. Oyler, and M.D. Donohue, *A critical analysis of paddlewheel-driven raceway ponds for algal biofuel production at commercial scales*. Algal Research, 2014. **4**: p. 76-88 DOI: 10.1016/j.algal.2013.11.007.

71. Julius S. Bendat, A.G.P., *Random Data: Analysis and Measurement Procedures*. Wiley Series in Probability and Statistics. 2010: Wiley Interscience. 640.

Appendix A – Mesh independence test

For the vertical flow geometry four meshes with different element sizes were tested. Table 7 summarizes the characteristics of the various grids analysed. The parameters used to assess the independence of the results on the grid were the velocity at the periodic boundary conditions surface and the wall shear stresses. These parameters are also shown in Table 7. Accordingly, Figure 27 shows the results obtained for each mesh studied.

Table 7. Element size, number of elements, velocity, u, and wall shear stresses, τ, for each mesh studied.

	Mesh02	Mesh01	Mesh005	Mesh0035
Element size /m	0.02	0.01	0.005	0.0035
Number of elements	700	1898	5800	10611
$u/\mathrm{m \cdot s^{-1}}$	0.2896	0.2889	0.2885	0.2884
τ/N	0.1898	0.1898	0.1898	0.1896

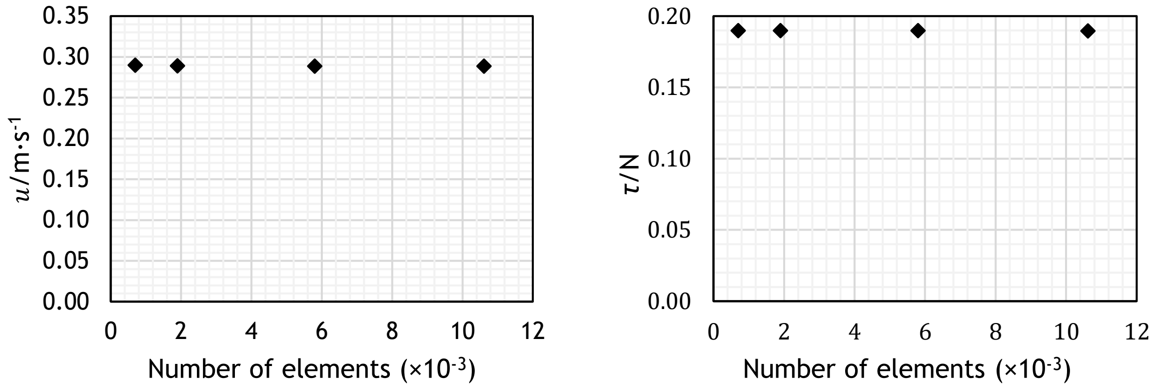

Figure 27. Velocity, u, and wall shear stresses, τ, for each mesh studied.

The results are very similar, i.e., do not strongly depend on the mesh's refinement level, as Figure 27 shows. For example, Mesh005 presents an error lower than 0.1 % in relation to the most refined mesh, regarding both parameters. Therefore, as the simulations were not very time-consuming, it was decided to use Mesh005 to obtain a good level of accuracy.

Appendix B - Δp assessment

The variation of the average velocity with the $\Delta p/L$ was studied for the case without roughness, as shown in Figure 28.

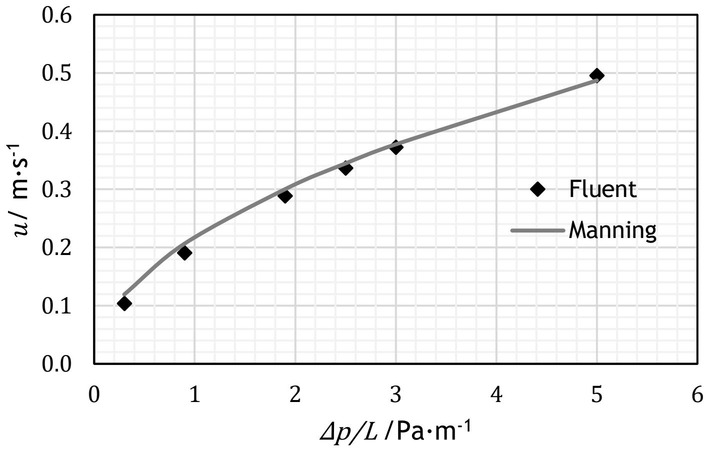

Figure 28. Comparison between Fluent and Manning's equation velocity.

Figure 28 shows that the values determined with RANS k-ε and Manning's equation are very similar. There were no notorious differences between the results obtained from CFD and those determined by the Manning equation. So, the Manning equation seems to provide a good estimate of the velocity in this type of flows. However, the simulation of this section does not consider the behaviour of the flow in the raceway U-turn. Therefore, it must be considered that Manning's equation represents an oversimplified approach that can be quite useful in simple geometries without space dependence. Nonetheless, in some cases, the estimation provided by Manning's equation may not be so accurate, hence the great usefulness of CFD tools, where it is possible to predict the flow behaviour independently of the geometry.

Furthermore, it can be observed that the $\Delta p/L$ and the average velocity of the fluid are proportional, i.e., when the velocity increases, the pressure drop along the flow also increases, which is in accordance with the turbulence theory where head loss scales quadratically with velocity. Thus, when the velocity is incremented, the turbulent kinetic energy increases as well as the turbulent energy dissipation rate and, as a result, the pressure drop rises.

Appendix C – Stoke's law

A particle suspended in a liquid has two forces acting on it, the drag force and the force of gravity.

For a falling particle in dynamic equilibrium, i.e., at the terminal velocity, the drag force, F_D must equal the gravity force, F_g, that is given by the difference between the weight and buoyancy of the particle as follows

$$F_D = F_g = V_p(\rho_p - \rho_f)g \tag{C.1}$$

in which ρ_p is the particle density, ρ_f is the fluid density, and V_p is the volume of a particle.

The drag force is given by,

$$F_D = \frac{1}{2} C_D \rho A v_t^2 \tag{C.2}$$

where C_D is the drag coefficient, A is the projected area of the particle, and v_t is the particle's terminal velocity.

In Stoke's regime, the drag coefficient is given by $C_D = \frac{64}{Re}$. So, by substituting this in Equation C.1 and considering that the particles are spheres, one can obtain the particles' settling velocity

$$v_t = \frac{2}{9} \frac{(\rho_p - \rho_f) g r^2}{\mu_f} \tag{C.3}$$

where r is the particle radius and μ_f is the viscosity of the fluid.

Appendix D – Probability Density Function

The PDF of random data describes the probability of the data assuming a value within some defined range at any instant. In this case, the probability that the y position of a particle, $y(t)$, assumes a value between y and $y + \Delta y$ can be obtained by taking the ratio T_y/T_t, in which T_y is the total amount of time that a particle falls inside the range $(y,\ y + \Delta y)$ during an observation time T_t [71]. This ratio will approach an exact probability description as T_t approaches infinity, as described by,

$$Prob\,[y < y(t) \leq y + \Delta y] = \lim_{T \to \infty} \frac{T_\infty}{T_t} \tag{D.1}$$

Appendix E - UVA spectrum

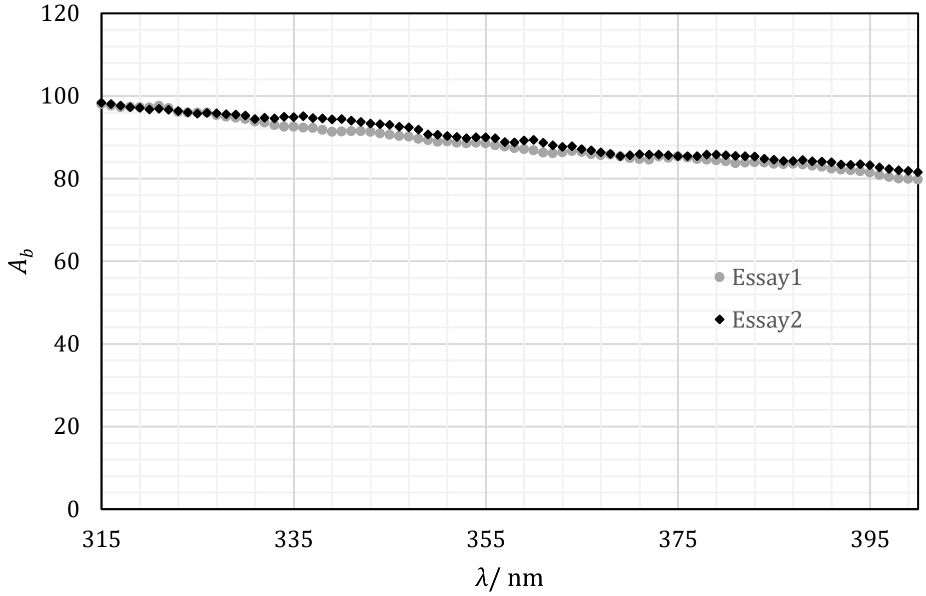

Figure 29. UVA spectrum of WAS for the two tests performed.

Appendix F - Sliding mesh model

The sliding mesh model is a specific case of general dynamic mesh motion. The formulation of this special case is rigid, i.e., all cells retain their original shape and volume. As so, the conservation equation for the sliding mesh model for a general scalar, φ , is given by,

$$\frac{\partial}{\partial t}\int_V \rho\varphi dV + \int_{\partial V} \rho\varphi(\vec{u} - \overrightarrow{u_g}) \cdot d\vec{A} = \int_{\partial V} \Gamma\nabla\varphi \cdot d\vec{A} + \int_V S_\varphi dV \qquad \text{(F.1)}$$

where $\vec{u}$ is the flow velocity vector, $\overrightarrow{u_g}$ is the mesh velocity of the moving mesh, Γ is the diffusion coefficient, S_φ is the source term of φ, V is an arbitrary control volume with a moving boundary, and dV represents the boundary of the control volume.

The time derivative term in Equation F.1 can be written using a first order backward difference, as follows,

$$\frac{\partial}{\partial t}\int_V \rho\varphi dV = \frac{[(\rho\varphi)^{n+1} - (\rho\varphi)^n]\, V}{\Delta t} \qquad \text{(F.2)}$$

where n and $n + 1$ denote the respective quantity at the current and next time level, respectively [60].

Appendix G - Torque

The torque over the paddlewheels, $\overrightarrow{T_r}$, is computed by assuming the cross products of the pressure and viscous force vectors for each face with the moment vector $\overrightarrow{r_{AB}}$ as follows,

$$\overrightarrow{T_r} = \overrightarrow{r_{AB}} \times \overrightarrow{F_p} + \overrightarrow{r_{AB}} \times \overrightarrow{F_v} \tag{G.1}$$

in which A is the specified moment centre, B is the force origin, $\overrightarrow{F_v}$ is the viscous force vector and $\overrightarrow{F_p}$ is the pressure force vector given by,

$$\overrightarrow{F_p} = \sum_{i=1}^{n} (p - p_{ref})\, A\hat{n} \tag{G.2}$$

p_{ref} represents a reference pressure that is used to normalize the cell pressure and reduce round-off errors, n is the number of faces, A is the area of the face and $\hat{n}$ is the unit normal to the face [60]. Figure 30 illustrates the explanation before.

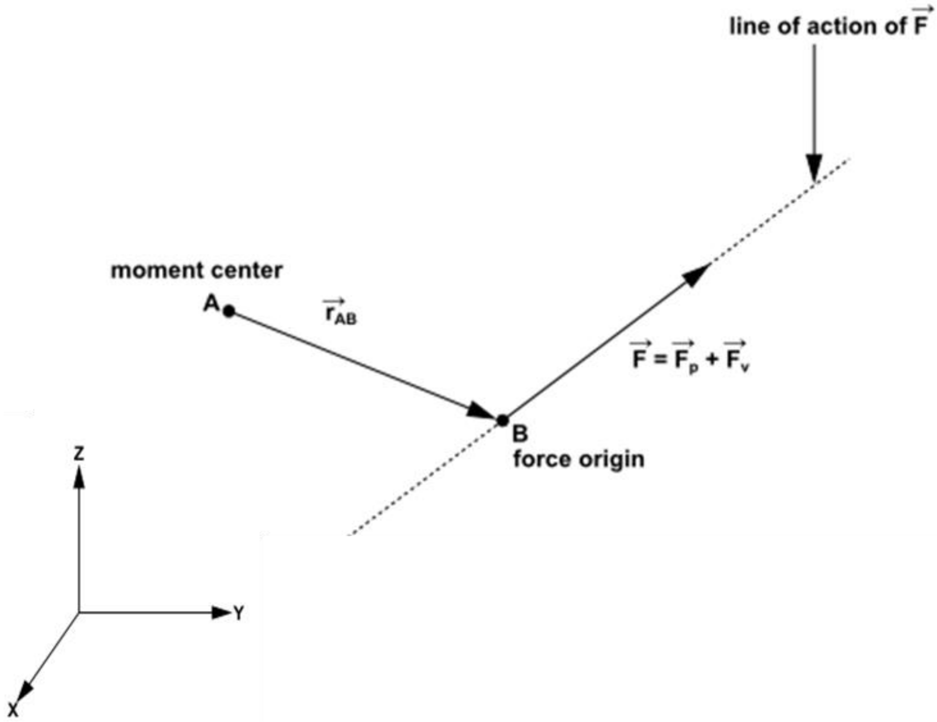

Figure 30. Moment about a specified moment centre.